ChemComm

ROYAL SOCIETY OF CHEMISTRY

REVIEW ARTICLE

View Article Online
View Journal | View Issue

Check for updates

Cite this: *Chem. Commun.*, 2026, **62**, 10100

Rise of high-entropy MXenes in electrocatalysis for sustainable energy conversion

Muhammad Yousuf, Xiaopeng Liu, Connor W. Schroeder, Jonathan Tjioe, Yurui Liu and Yue Wu*

High-entropy (HE) MXenes constitute an emerging class of two-dimensional carbides and carbonitrides that combine the tunable surface chemistry and metallic conductivity of MXenes with the configurational entropy, lattice distortion and multi-metal interactions of high-entropy materials (HEMs). This review presents the fundamental structural and thermodynamic features of MXenes, HEMs and HE-MXenes, establishing how multi-component M-sublattices and mixed terminations create ensembles of adsorption sites relevant to electrocatalysis. Progress in the synthesis and structural design of HE-MXenes is summarised, covering design of HE-MAX precursors, etching and delamination strategies, and advanced structural and chemical characterisation that enable control over composition, defects and surface terminations. The current understanding of electronic structure, active-site motifs and defect/termination chemistry in HE-MXenes is discussed, with emphasis on how lattice distortion and local coordination govern adsorption energetics. On this basis, recent advances in HE-MXenes and HE-MXene-based heterostructures for hydrogen evolution and oxidation, oxygen evolution and reduction, and other electrochemical conversion reactions, particularly CO_2 and N_2 reduction, are critically assessed against conventional MXenes, high-entropy catalysts and noble-metal systems. Furthermore, key challenges and opportunities are identified, including synthetic control of multi-metal distributions, coupled termination–defect engineering, *operando* interrogation of active phases and predictive modelling of high-dimensional composition space, with a view to guiding the rational deployment of HE-MXenes in sustainable electrocatalytic energy-conversion technologies.

Received 22nd January 2026,
Accepted 24th April 2026

DOI: 10.1039/d6cc00413j

rsc.li/chemcomm

Department of Chemical and Biological Engineering, Iowa State University, 618 Bissell Road, Ames, IA 50011, USA. E-mail: yuewu@iastate.edu

Muhammad Yousuf

Muhammad Yousuf is a PhD candidate and graduate assistant in the Department of Chemical and Biological Engineering, Iowa State University. He worked as a graduate research assistant at the School of Mechanical Engineering and Automation, Beihang University (2018–2019) and subsequently joined the Institute of Engineering Thermophysics, Chinese Academy of Sciences (2020–2025). He received his MSE. from the University of Chinese Academy of Sciences (2024) and BE from Beihang University (2019). His current research focuses on advanced materials and catalytic systems for electrocatalytic applications in low-carbon energy conversion, with particular emphasis on nitrogen-related electrochemical reactions, methane oxidation, and sustainable energy technologies.

Xiaopeng Liu

Xiaopeng Liu received her PhD in Chemical Engineering from Iowa State University. Her research focuses on MXene-based electrocatalysis for sustainable energy conversion, with emphasis on metal–support interactions and high-current-density hydrogen evolution. She has developed MXene-based catalysts and electrolyzers to probe structure–activity relationships under practical operating conditions. She is currently a Postdoctoral Fellow at the Texas Materials Institute, The University of Texas at Austin, working on data-driven and high-throughput approaches for the discovery of advanced functional materials.

1. Introduction

Electrochemical energy conversion technologies, including water electrolysis, fuel cells, metal–air batteries, and the electroreduction of CO_2, are central to the transition towards low-carbon energy systems.[1–5] Their practical deployment, however, is still constrained by sluggish multi-electron reaction kinetics and by the cost, scarcity, and sometimes limited durability of conventional noble-metal catalysts.[6–9] Considerable effort has therefore been devoted to the discovery of earth-abundant electrocatalysts that combine high intrinsic activity with long-term stability and compatibility with device-level operating conditions. Two concepts have recently converged in this context. The first is the emergence of two-dimensional MXenes as a versatile family of electrically conductive carbides and nitrides with tunable surface chemistry. The second is the high-entropy materials (HEMs) paradigm, in which several principal elements are mixed in near-equimolar ratios to exploit configurational entropy, lattice distortion, and ‘‘cocktail’’ effects to stabilise single-phase solids with emergent properties.[10–12] Their intersection, high-entropy (HE) MXenes, is now opening an unusually rich design space for electrocatalysts.

Since the initial isolation of $Ti_3C_2T_x$ in 2011 by selective etching of Ti_3AlC_2 MAX phases, the MXene family has expanded rapidly,[13] as summarised in Fig. 1. Successive advances in MAX-phase chemistry, etching and delamination protocols, and post-synthetic modification have produced dozens of $M_{n+1}X_nT_x$ compositions with diverse transition-metal sublattices, X = C and/or N, and mixed surface terminations (T_x = –O, –OH, –F, –Cl, –S, *etc.*). MXenes combine metal-like electronic conductivity with a layered architecture in which interlayer spacing, defect density, and heterostructure interfaces can be engineered almost independently. This has enabled applications ranging from supercapacitors and batteries to electromagnetic

Connor W. Schroeder

Connor W. Schroeder is a PhD Candidate in the Department of Chemical and Biological Engineering at Iowa State University. His research interests focus on the synthesis, characterization, and optimization of high entropy alloy materials for mechanical, electrical, thermal, and catalytic applications. His work includes building a crystallographic understanding of single-phase solid solution high entropy materials and the impact of entropic engineering on material performance.

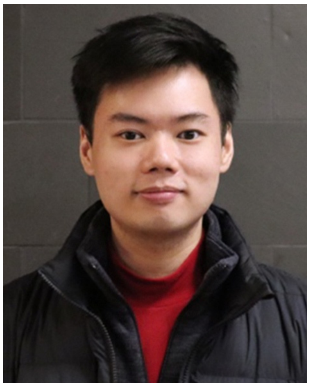

Jonathan Tjioe

Jonathan Tjioe is currently a PhD student in the Department of Chemical and Biological Engineering at Iowa State University. His research focuses on using MXenes as catalyst supports to upgrade waste plastics and biomass into higher-value products, including fuels, lubricants, and fine chemicals. His work includes the development of transition-metal single-atom catalysts by leveraging the strong metal–support interactions of MXenes. He received his bachelor's degree in Chemical Engineering from Universitas Indonesia.

Yurui Liu

Yurui Liu is a PhD candidate in Chemical and Biological Engineering at Iowa State University. Her research focuses on thermal transport in two-dimensional materials, with particular emphasis on MXenes, using advanced optical characterization techniques such as Energy Transport Raman spectroscopy. Her work seeks to elucidate heat conduction mechanisms at the micro- and nanoscale and to provide fundamental insight into the thermal behavior of low-dimensional materials. Through this research, she aims to advance the understanding and design of materials for thermal management applications.

Yue Wu

Yue Wu is the Herbert L. Stiles Professor in the Department of Chemical and Biological Engineering at Iowa State University. He received his PhD in Chemistry from Harvard University (2006) and completed postdoctoral research as a Miller Fellow at the University of California, Berkeley (2006–2009). He joined Purdue University (2009) and moved to Iowa State University (2014). His research focuses on advanced materials and catalytic systems for energy and sustainability. He has received several recognitions, including the DuPont Young Professor Award and the AIChE Nanoscale Science and Engineering Young Investigator Award.

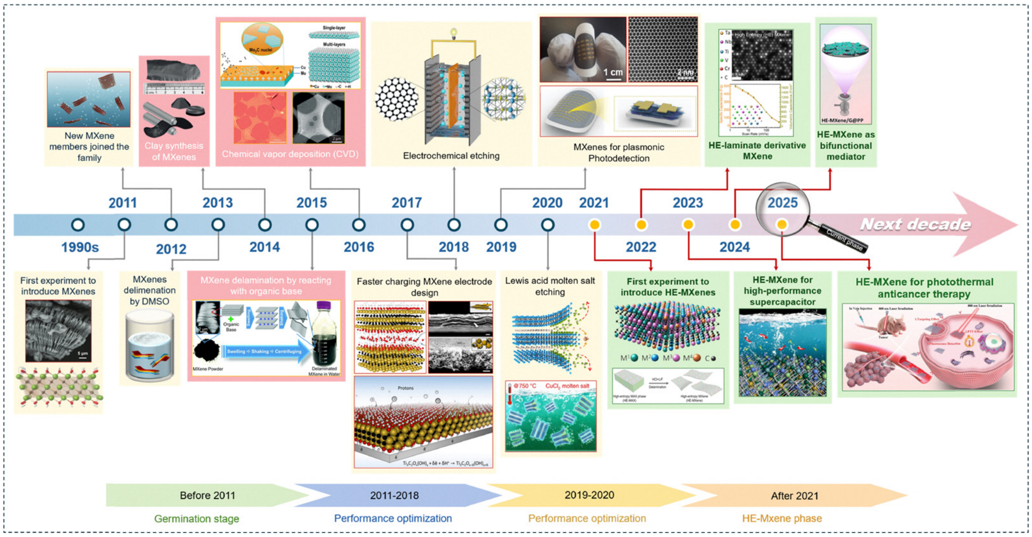

Fig. 1 Timeline of MXene synthesis and structural evolution (2011–2025), highlighting milestones in etching/delamination, assembly into architectures, and the emergence of HE-MAX phases and HE-MXenes.[13–15,22,29,39,128–135] Reproduced with permission from ref. 13, copyright 2011, John Wiley and Sons. Reproduced with permission from ref. 14, copyright 2023, Elsevier. Reproduced with permission from ref. 15, copyright 2024, American Chemical Society. Reproduced with permission from ref. 22, copyright 2021, American Chemical Society. Reproduced with permission from ref. 29, copyright 2021, John Wiley & Sons. Reproduced with permission from ref. 39, copyright 2022, American Chemical Society. Reproduced with permission from ref. 128, copyright 2025, John Wiley & Sons. Reproduced with permission from ref. 129, copyright 2015, Royal Society of Chemistry. Reproduced with permission from ref. 130, copyright 2015, Springer Nature. Reproduced with permission from ref. 131, copyright 2014, Springer Nature. Reproduced with permission from ref. 132, copyright 2019, John Wiley & Sons. Reproduced with permission from ref. 133, copyright 2017, Springer Nature. Reproduced with permission from ref. 134, copyright 2020, Springer Nature. Reproduced with permission from ref. 135, copyright 2019, Springer Nature.

shielding, photothermal therapy, and heterogeneous catalysis.[14–17] In parallel, high-entropy alloys, oxides, carbides, and chalcogenides have demonstrated that multi-component lattices can stabilise disordered yet single-phase structures, suppress phase segregation, and generate broad distributions of adsorption sites that are favourable for reactions such as the hydrogen evolution reaction (HER), oxygen evolution and reduction (OER/ORR), CO_2 reduction (CO_2RR), and nitrogen reduction (NRR).[18–20]

Extending the high-entropy concept to MXenes creates HE-MXenes, in which four or more transition metals occupy the M-sublattice of the parent MAX phase in near-equimolar ratios. Beyond single-metal MXenes, the design space has expanded through M-site mixing (random solid solutions and ordered double-M phases) and ordered vacancy motifs, which demonstrated that local coordination and surface chemistry can tune adsorption energetics while preserving the layered scaffold (Fig. 2).[21] HE-MXenes occupy the top tier of this hierarchy: they retain the $M_{n+1}X_n$ scaffold but distribute four or more transition metals across the M-sublattice, often in near-equimolar ratios, such that adsorption sites are defined by statistically varying metal neighbourhoods and their associated electronic structures. In later sections, this diversity is treated explicitly in terms of distributions of adsorption free energies and their impact on activity and selectivity.[7] Early examples such as $TiVNbMoC_3T_x$, $TiVCrMoC_3T_x$ and related multi-metal M_4C_3 and M_2C systems showed that configurational entropy can stabilise layered carbides against phase separation, and that the resulting MXenes preserve high electronic conductivity while exhibiting enhanced structural robustness and rich local electronic heterogeneity.[22–24] In HE-MXenes, lattice distortion, multi-metal bonding and heterogeneous surface terminations collectively generate a continuum of local environments and adsorption energies rather than a single "average" active site. This multiplicity of sites can increase the probability of finding near-optimal binding energies for different reaction intermediates on the same surface, while entropy-stabilised structures may improve tolerance to oxidation, dissolution and mechanical stress under operation.[11,12,21–24] To date, much of the HE-MXene literature has focused on electrochemical energy storage, especially Li-, Na- and K-ion batteries, supercapacitors and lithium–sulfur systems, where HE-MXenes act as high-surface-area hosts, conductive scaffolds or polysulfide mediators.[25–29] In contrast, systematic studies of HE-MXenes as electrocatalysts for key energy-conversion reactions are only beginning to emerge, even though the broader high-entropy electrocatalyst community has already shown that multicomponent oxides, sulfides and alloys can achieve outstanding HER, OER, ORR, CO_2RR and NRR performance by using entropy-driven stabilisation of active phases, suppression of competing pathways and deliberate tuning of adsorption-energy distributions.[18–20,30,31]

Building on broader progress in high-entropy electrocatalysts, HE-MXenes can be viewed as an emerging platform for sustainable electrochemical energy conversion. Fig. 3A connects these materials concepts to a broader sustainability landscape in which electrolysers, fuel cells and other HE-MXene–based devices operate within low-carbon infrastructure. Fig. 3B extends this perspective to an integrated renewable-hydrogen energy cycle, in which HE-MXene electrocatalysts facilitate the conversion of intermittent solar, wind and hydro resources into chemical fuels and back to electricity

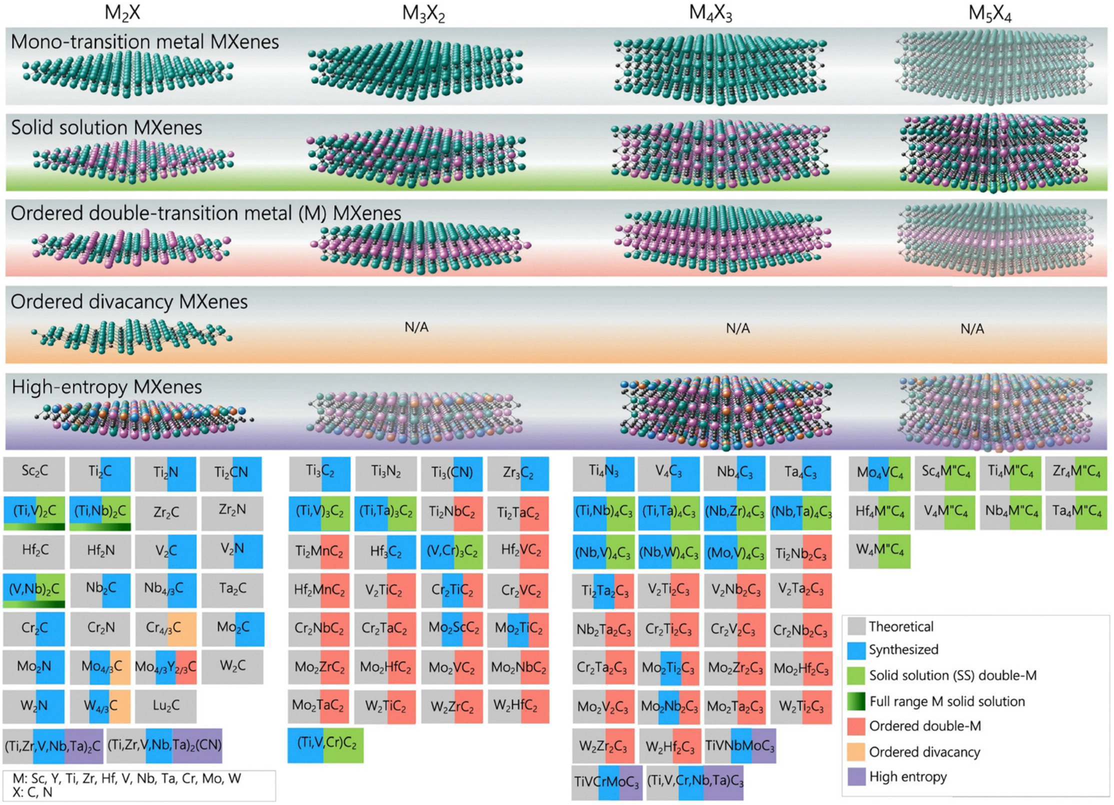

Fig. 2 Structural hierarchy of MXenes from single-metal compositions to HE-MXenes, highlighting the $M_{n+1}X_n$ backbone, typical terminations (T_x) and representative adsorption motifs. Reprinted with permission from ref. 21, copyright 2018, Springer Nature.

via water splitting and fuel cells. A bibliometric survey of the literature reveals that publications explicitly focused on HE-MXenes have risen sharply since 2021 (Fig. 3C), underscoring both the youth of the field and the rapidly growing interest in exploiting high-entropy design within the MXene family for energy-relevant electrocatalysis.

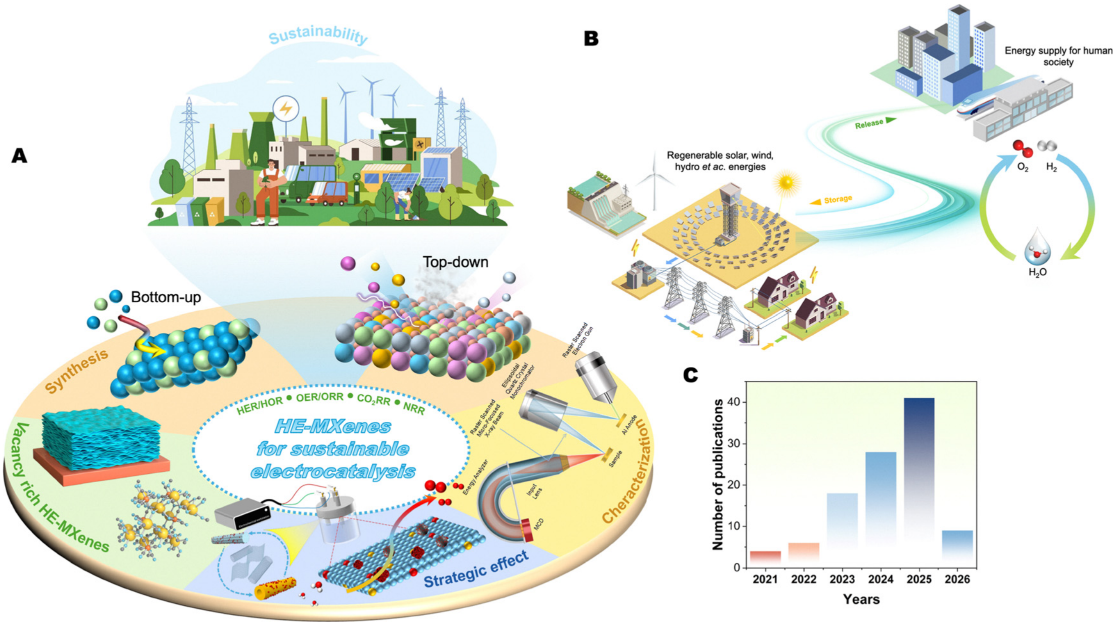

Fig. 3 Conceptual overview of the emerging role of HE-MXenes in electrocatalysis for sustainable energy conversion. (B) Schematic illustration of the renewable-electricity–hydrogen–electricity cycle relevant to HE-MXene-enabled energy conversion. (C) Statistics on the number of publications related to HE-MXenes since 2021 (Data from Web of Science, collected on 10 Feb 2026).

The aim of this review is therefore to provide a coherent picture of how HE-MXenes can be designed, understood and implemented as electrocatalysts for sustainable energy conversion, rather than as a simple extension of either MXenes or HEMs alone. Entire chain from synthesis of HE-MAX precursors and etching/delamination into HE-MXenes, through control of vacancies and terminations, to structural design, mechanistic understanding and device-level integration for HER/HOR, OER/ORR, CO_2RR, NRR, and related reactions is explicitly considered (Fig. 3A). Section 2 revisits the fundamentals of HEMs and HE-MXenes, setting the thermodynamic and structural background. Section 3 discusses synthesis and structural design of HE-MXenes, emphasising routes that enable control over composition, defects and surface terminations. Section 4 examines electronic structure, active sites and theoretical modelling, with a focus on how multi-metal and termination-induced heterogeneity can be captured in descriptor-based frameworks. Sections 5 and 6 survey the current state of HE-MXenes in hydrogen- and oxygen-related electrocatalysis, while Section 7 extends the discussion to other electrochemical conversion reactions such as CO_2RR and NRR. Finally, Section 8 summarises the main challenges and opportunities for HE-MXenes to evolve from a promising materials concept into a robust platform for electrocatalysis in future sustainable energy technologies.

2. Fundamentals of MXenes, high-entropy materials and high-entropy MXenes

2.1 High-entropy materials and their electrocatalytic features

HEMs are multicomponent solid solutions in which four or more elements share a crystallographically equivalent sublattice in (approximately) equimolar ratios. Their design is usually framed in terms of the Gibbs free energy of mixing,

$$\Delta G_{\mathrm{mix}} = \Delta G_{\mathrm{mix}} - T\Delta S_{\mathrm{mix}},$$

with the configurational entropy

$$\Delta S_{\mathrm{mix}} = -R\sum_{i=1}^{N} c_i \ln c_i,$$

where ΔG_{mix}, is the Gibbs free energy of mixing, ΔH_{mix} is the enthalpy of mixing, ΔS_{mix} is the entropy of mixing, T is the absolute temperature (K), R is the gas constant, c_i is the atomic (molar) fraction of component i, i indexes the components, N is the total number of components, and ln denotes the natural logarithm. The ''entropy parameter.''

$$\Omega = \frac{T_{\mathrm{m}}\Delta S_{\mathrm{mix}}}{|\Delta H_{\mathrm{mix}}|},$$

uses the average melting point T_{m} of the elements (K) to gauge whether entropy can compensate the enthalpy of mixing; $|\Delta H_{\mathrm{mix}}|$ denotes the absolute value of the mixing enthalpy. Empirical analysis of high-entropy alloys (HEAs) shows that disordered solid solutions are favoured when the mixing enthalpy lies roughly in $-15 < \Delta H_{\mathrm{mix}} < 5\ \mathrm{kJ\ mol^{-1}}$, the atomic size mismatch δ (typically reported as a percentage measure of the dispersion in atomic radii among constituents) is below $\sim$5%, and $\Omega > 1$; systems with $\Delta S_{\mathrm{mix}} > 1.5R$ are commonly classified as ''high-entropy''. These criteria, originally formulated for bulk HEAs, have since been extended to ceramics and low-dimensional systems and provide a quantitative starting point for designing high-entropy carbides, nitrides, oxides and, by extension, HE-MXenes.

Yeh and co-workers rationalised HEM behaviour in terms of four ''canonical'' high-entropy effects: a thermodynamic high-entropy effect, lattice distortion, sluggish diffusion and the ''cocktail'' effect.[23] In brief, the thermodynamic effect stabilises single-phase solid solutions that would otherwise decompose; lattice distortion introduces local strain and modifies bond lengths/angles; sluggish diffusion reflects the complex energy landscape for migrating atoms in a disordered lattice; and the cocktail effect refers to emergent properties arising from multi-element synergy rather than from any individual component. For electrocatalysis, these effects are not merely conceptual: they control how many distinct local environments exist at the surface, how stable those environments are under potential cycling, and how activity and durability can be combined in a single phase. Their practical impact has been most clearly demonstrated so far in metallic HEAs in Fig. 4. Oxidative corrosion of MXenes typically initiated at edges, vacancies, and termination defects, where O/OH species adsorbed and subsequently enabled oxygen ingress together with metal migration/leaching that nucleated oxide/(oxy)hydroxide domains. In HE-MXenes, configurational-entropy stabilisation, lattice distortion, and sluggish diffusion could collectively retard this process by (i) reducing the driving force for element segregation into distinct oxide phases and (ii) increasing migration barriers for both metal and oxygen species in the disordered lattice. As a result, oxide growth and preferential leaching of individual metals could be kinetically suppressed, and compositionally complex surface (oxy)carbide/(oxy)hydroxide layers may form that further impede oxidant transport. Although systematic atomic-scale verification for HE-MXenes remained limited, this framework provided a mechanistic basis for the corrosion/oxidation tolerance often associated with high-entropy compositions.

Among the different high-entropy electrocatalyst families, metallic HEAs provide the clearest precedent for how complex solid solutions can be rationally exploited in energy conversion. Batchelor *et al.* combined density functional theory (DFT) based adsorption–energy models with composition-spread Ag–Ir–Pd–Pt–Ru thin-film libraries and scanning droplet-cell measurements to build a closed, data-driven discovery loop, in which predictions, combinatorial synthesis and high-throughput characterisation iteratively refine one another and identify activity maxima for the ORR in a vast composition space (Fig. 4A and B).[32] This work shows that the statistical distribution of adsorption sites on high-entropy surfaces can be treated explicitly and optimised, rather than sampled empirically, and it provides a methodological template that is directly transferable to high-entropy design on MXene basal planes. A complementary example is provided by Pt-optimised AuAgCuPdPt

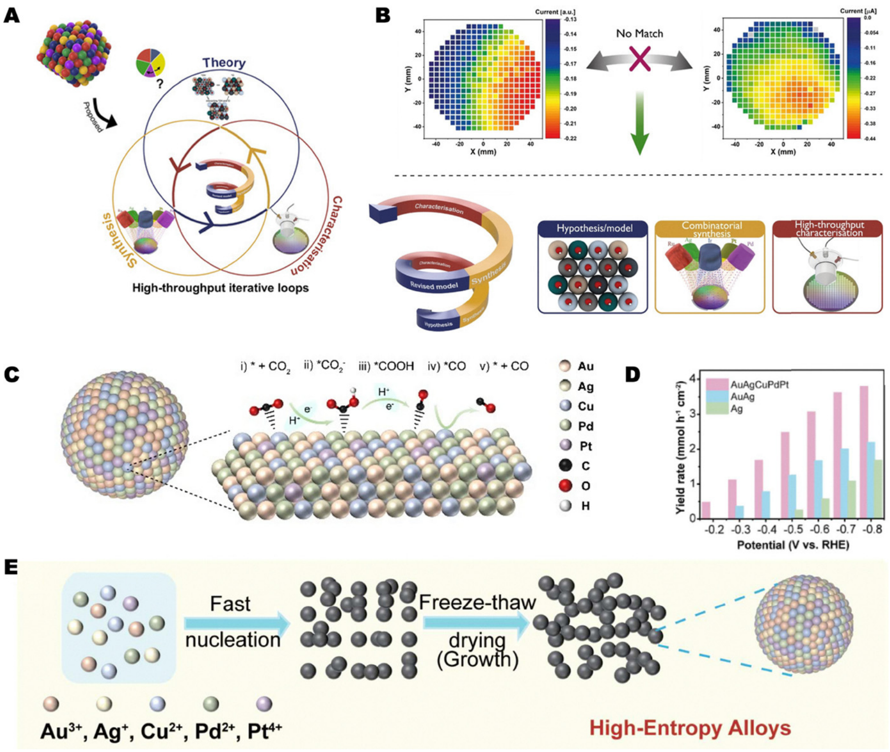

Fig. 4 HEAs as a model platform for data-driven electrocatalyst discovery and CO_2 reduction. (A) Concept of complex solid-solution HEAs with millions of distinct surface sites, highlighting the need to integrate theory, synthesis and characterisation in a high-throughput iterative loop. (B) Schematic of the computational–experimental discovery cycle and comparison between predicted and measured ORR activity maps on a composition-spread thin-film library. Reprinted with permission from ref. 32, copyright 2020, John Wiley & Sons. (C) Schematic representation of CO_2 reduction to CO on a multimetal HEA surface *via* *CO_2, *COOH and *CO intermediates. (D) Potential-dependent CO yield rates for AuAgCuPdPt HEAs compared with AuAg and Ag catalysts. (E) Wet-chemical synthesis route to AuAgCuPdPt HEA nanoparticles *via* rapid nucleation followed by freeze–thaw growth. Reprinted with permission from ref. 33, copyright 2025, Springer Nature.

HEAs for CO_2-to-CO conversion (Fig. 4C–E): Li and co-workers achieved faradaic efficiencies (FE) for CO above 90% over a wide potential window and significantly higher CO yield rates than monometallic Ag or bimetallic AuAg, while maintaining a single fcc phase and excellent stability in both flow-cell CO_2RR and Zn–CO_2 battery operation.[33] *In situ* Raman and ATR-FTIR spectroscopy revealed that the multimetal ensemble stabilises *CO_2^- and *COOH intermediates, weakens *CO binding and promotes water dissociation, thereby suppressing HER and enabling selective CO formation, an archetypal demonstration of how lattice distortion and cocktail effects in high-entropy systems translate into practical gains in electrocatalytic activity and selectivity.

Taken together, these studies yield several general lessons that are particularly relevant to the emerging role of HE-MXenes in electrocatalysis. First, successful high-entropy design requires balancing configurational entropy, mixing enthalpy and size mismatch so that genuine single-phase solid solutions are obtained rather than multiphase mixtures, exactly the challenge faced when selecting element sets for HE-MAX and HE-MXene systems. Second, cation and anion disorder, including vacancies and mixed-valence states, are central to both activity and stability; in perovskite and spinel HEMs, oxygen defects and multi-metal synergy correlate with enhanced NRR and OER performance, and an analogous role can be anticipated for vacancy and termination disorder in HE-MXenes. Third, the complexity of HEMs demands rigorous structural and electronic characterisation (XRD/Rietveld, electron microscopy, XPS, XANES/EXAFS) to confirm true single-phase behaviour and to resolve local coordination environments. Finally, high-entropy electrocatalysis has shown that composition–structure–function relationships must be established mechanistically rather than by empirical screening alone. This perspective directly underpins later sections, where high-entropy design principles are transplanted to the two-dimensional MXene platform for sustainable energy-conversion reactions.

2.2 High-entropy MXenes as 2D high-entropy materials

HE-MXenes belong to the emerging class of 2D-HEMs, which also includes oxides, chalcogenides, hydroxides and other carbides.[34,35] These systems represent the latest step in the broader development of entropy-stabilised multi-principal-element materials, from 3D HEAs and ceramics to layered structures in which configurational entropy is implemented within an atomically thin framework (Fig. 5).[24,36] In this context, HE-MXenes can be viewed as 2D carbide/carbonitride analogues in which the M-sublattice of the $M_{n+1}X_n$ slab hosts

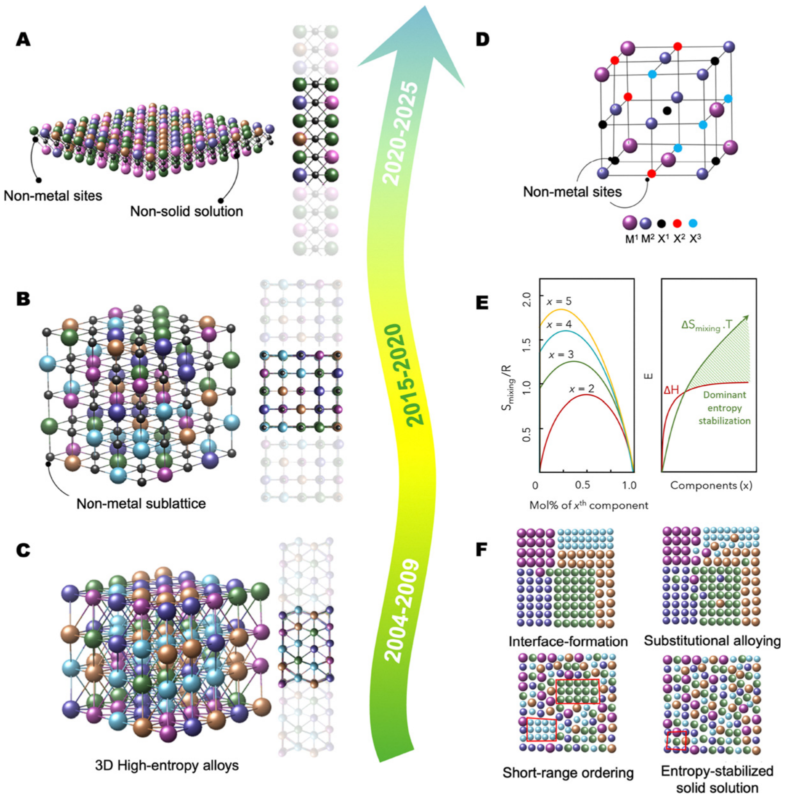

Fig. 5 Evolution of entropy-stabilised multi-principal-element materials from 3D HEAs/ceramics to 2D HEMs, providing the conceptual basis for HE-MXenes. (A–D) Representative structural models of multi-principal-element materials with increasing dimensional and compositional complexity. (E) Schematic thermodynamic basis of entropy stabilisation. (F) Representative disorder motifs, including interface formation, substitutional alloying, short-range ordering, and entropy-stabilised solid solutions. Reproduced with permission from ref. 36, copyright 2021, AAAS.

a near-equimolar mixture of early transition metals (*e.g.* Ti, V, Nb, Mo, Cr, Zr, Ta), while the X (C/N) sublattice and surface terminations can also display compositional complexity.[29] Compared with binary or ternary MXenes, this multicomponent character introduces additional configurational degrees of freedom that can be used to adjust local bonding, electronic structure and, ultimately, electrocatalytic response.[37]

From a thermodynamic perspective, HE-MXenes follow the same principle as bulk high-entropy ceramics: near-equimolar mixing of several cations on a crystallographically equivalent sublattice increases the molar configurational entropy and can stabilise a single-phase solid solution against decomposition.[37] In the 2D limit, this entropy originates primarily from mixing on the metallic M-sublattice, but it may also arise from disorder on the non-metal sublattice (C/N) and from statistical distributions of surface terminations (O, OH, F, Cl, S, *etc.*).[38] HE-MXenes therefore combine several levels of disorder: chemical disorder within each M layer, possible carbonitride disorder on the X sublattice, and termination disorder on both faces of the sheet, producing a spectrum of local coordination environments, bond lengths, and electronic states.[29,35] This hierarchical disorder gives rise to lattice distortions, electronic inhomogeneity and modified orbital hybridisation, features that are central to the emerging electrocatalytic behaviour of HE-MXenes. These effects have been directly observed in representative HE-MXenes. Du *et al.* synthesised high-entropy M_2CT_x MXenes by etching a $(Ti_{1/5}V_{1/5}Zr_{1/5}Nb_{1/5}Ta_{1/5})_2AlC$ HE-MAX phase and showed that the transition metals are homogeneously dispersed within the MX slab at the atomic scale, consistent with a solid-solution character.[29] The size mismatch among the five cations induced significant lattice distortions and internal strain, which strongly influenced Li nucleation and growth and enabled dendrite-free plating/stripping at the HE-MXene interface.[29] Similar local distortions and expanded in-plane lattice parameters have been reported for other HE-MXenes when larger cations such as Nb, Zr and Ta are introduced into Ti-based frameworks, leading to measurable changes in the (100)/(010) spacings and selected-area electron diffraction patterns.[38]

Building on this, Nemani and co-workers realised high-entropy 413 MXenes $TiVNbMoC_3T_x$ and $TiVCrMoC_3T_x$ by etching the corresponding HE-MAX precursors. High-resolution XRD confirmed that the M_4AlC_3 MAX phases were single-phase with lattice parameters comparable to non-high-entropy analogues, while atomic-resolution STEM/EDS mapping revealed uniform distributions of Ti, V, Nb and Mo (or Cr) across the MXene flakes without detectable clustering.[22] XPS depth profiling showed near-equimolar metal ratios through the sheet thickness and a complex mixture of metal–C/O/F bonds and oxidation states, reflecting the multi-metal surface chemistry. Du *et al.* first extended this concept to carbonitride MAX phases by synthesising a high-entropy carbonitride MAX, $(Ti_{1/3}V_{1/6}Zr_{1/6}Nb_{1/6}Ta_{1/6})_2AlC_xN_{1-x}$, and demonstrating that the five metals form a solid solution on the M sublattice; etching then yielded high-entropy carbonitride MXenes with homogeneous multi-metal distributions.[29] Subsequently, Zhou *et al.* showed that careful control of the M/Al/C ratios and sintering conditions yields single-phase high-entropy laminate MAX precursors and their two-dimensional derivatives without competing carbides or intermetallics.[39] Etman and co-workers further reported $Ti_{1.1}V_{0.7}Cr_xNb_{1.0}Ta_{0.6}C_3T_z$ freestanding films that combine multi-metal mixing with good mechanical integrity and promising charge-storage performance.[40] Together, these studies establish that HE-MXenes can be synthesised reproducibly in both M_2X- and M_4X_3-type structures across a range of carbide and carbonitride chemistries.

Electronic–structure calculations complement these experimental observations. High-throughput DFT and Monte Carlo simulations for $TiVNbMoC_3$ and $TiVCrMoC_3$ indicate that, although the overall compositions are equimolar, energetically favoured configurations can exhibit partial interlayer chemical ordering, with certain metals enriched at the outer layers and others stabilised in the inner ones.[41] This tendency becomes more pronounced at lower temperatures, but entropy-stabilised disordered configurations remain accessible at realistic synthesis temperatures, in agreement with experimental evidence for multi-metal occupation and selective etching behaviour.[38] From an electrocatalytic viewpoint, HE-MXenes thus provide a dense ensemble of inequivalent adsorption sites, each with slightly different local coordination and electronic structure. DFT studies on oxygen-terminated $TiVNbMoC_3$ have shown that the hydrogen adsorption free energy can be tuned within a narrow window around thermoneutrality by sampling different local metal environments on the same basal plane,[42] while spectroscopic analyses of high-entropy carbides and carbonitrides reveal a rich variety of $M–C–T_x$ and $M–N–T_x$ bonds with subtly shifted binding energies, indicating variations in metal–ligand covalency and charge density.[38,43] These ensemble and surface-chemistry effects, combined with the high in-plane conductivity of MXenes, underlie the enhanced and tunable electrocatalytic behaviour observed in HE-MXenes.[38,43]

Ultimately, HE-MXenes are best regarded as a subclass of functional two-dimensional HEMs in which configurational entropy is embedded within a layered carbide/carbonitride scaffold endowed with accessible, chemically active surfaces. Their development has established the synthetic feasibility, structural stability and homogeneous multi-metal distributions required for rational property optimisation, while theory and experiment agree that high-entropy mixing generates local strain, electronic heterogeneity and a spectrum of adsorption environments that can be exploited to engineer electrocatalytic performance beyond that of simpler MXene chemistries.[18,44] Table 1 compiles the experimentally realised HE-MXenes reported so far and highlights how this material family has already moved beyond purely structural demonstrations into functional electrocatalysis and energy storage. $TiVNbMoC_3$ and $TiVCrMoC_3$ derived from quinary HE-MAX phases deliver high and stable capacities as Li- and Na-ion battery anodes,[27] while $Ti_{1.1}V_{1.2}Cr_{0.8}Nb_{1.0}Mo_{0.9}C_4T_x$ and $Ti_{1.1}V_{0.7}Cr_xNb_{1.0}Ta_{0.6}C_3T_z$ exhibit competitive capacitances and cycling stability in alkaline and acidic supercapacitors.[14,39,40] In parallel, $(Ti_{1/5}V_{1/5}Zr_{1/5}Nb_{1/5}Ta_{1/5})_2CT_x$ promotes uniform Li plating with millivolt-scale nucleation overpotentials,[29] and $TiVNbMoC_3$-based architectures act as efficient sulfur hosts and separator mediators in Li–S batteries, enabling long-term cycling at practical loadings.[15,45] More recently, HE-MXenes have begun to serve as conductive, corrosion-resistant supports for multicomponent electrocatalysts, for example, in $V–Co_2P$@HE heterostructures for overall water splitting and in CuFeMnCoNi-NC/MXene anodes for anion-exchange membrane water electrolysers.[31,46] Together with HE-MXenes designed for electromagnetic-wave absorption and other functionalities,[43,47] these examples demonstrate that the HE-MXene concept is already technologically versatile, while also revealing that truly electrocatalysis-focused compositions remain relatively scarce.

3. Synthesis and structural design of high-entropy MXenes

3.1 Design principles for high-entropy MAX precursors

HE-MAX phases are the indispensable precursors for HE-MXenes and must be obtained as single-phase layered carbides or carbonitrides (most commonly M_4AlC_3 and M_3AlC_2 types) in which three to five early transition metals occupy the M sublattice in near-equimolar ratios, while the A and X sites remain relatively simple so that configurational entropy is concentrated on the metal lattice.[48] The key design requirement is that this multicomponent M sublattice forms a genuine solid solution instead of decomposing into mixtures of binary MAX phases, simple carbides or intermetallics. This demands compatibility in atomic radius, electronegativity and valence state, and an overall combination that lies within acceptable ranges of mixing enthalpy and atomic size mismatch while providing sufficient configurational entropy at the synthesis temperature.[48] DFT calculations for $TiVNbMoAlC_3$ and $TiVCrMoAlC_3$ showed that the corresponding four-metal M_4AlC_3 solid solutions have negative formation enthalpies and lie close to the convex hull when competing carbides and intermetallics are considered, whereas analogous three-metal compositions tend to split into multiple MAX phases.[22] Only when four equimolar metals are included does the $-T\Delta S$ term become large enough to stabilise a single-phase HE-MAX, a prerequisite for obtaining phase-pure HE-MXenes.[22,35]

Empirical criteria derived from bulk high-entropy carbides and oxides provide a practical starting point for such design.[27,35] Robust single-phase solid solutions are favoured when the atomic size mismatch on the disordered sublattice is modest and the configurational entropy exceeds the usual high-entropy threshold; translated to MAX phases, this means selecting M elements with similar metallic radii and comparable electronegativities, each of which is known to form conventional MAX phases with Al and C/N, and avoiding

Table 1 Summary of some recent experimentally reported HE-MXenes and their corresponding HE-MAX precursors used for electrocatalytic and energy-storage applications

HE-MAX	HE-MXene (support/host)	Purpose/role	MAX synthesis temp. (°C)	Reaction/device	Key performance (selected)	Ref.
$Ti_{1.1}V_{1.2}Cr_{0.8}Nb_{1.0}Mo_{0.9}AlC_4$	$Ti_{1.1}V_{1.2}Cr_{0.8}Nb_{1.0}Mo_{0.9}C_4T_x$ (M_5C_4)	High-capacitance HE-MXene for alkaline supercapacitors	1500	Supercapacitor (1 M KOH, three-electrode)	284.6 F g^{-1} at 1 A g^{-1}; 170 F g^{-1} at 10 A g^{-1}; reduced R_s and R_{ct} *vs.* Nb_2CT_x, V_2CT_x, $Ti_3C_2T_x$	14
$(Ti_{0.2}V_{0.2}Nb_{0.2}Mo_{0.2}W_{0.2})_3AlC_2$	$(Ti_{0.2}V_{0.2}Nb_{0.2}Mo_{0.2}W_{0.2})_3C_2T_x$	High-stability HE-MXene electrode for supercapacitors	1550	Supercapacitor (1 M H_2SO_4, three-electrode) and MXene-HF 72 h//AC asymmetric supercapacitor	158.43 F g^{-1} at 5 mV s^{-1}; 128.98 F g^{-1} at 0.5 A g^{-1}; electrode: 100% retention after 10 000 cycles at 10 A g^{-1}; device: 50.18 F g^{-1} at 1 A g^{-1}, 13.98 Wh kg^{-1}/163.35 W kg^{-1}, 98.7% retention after 10 000 cycles at 5 A g^{-1}	136
$TiVCrMoAlC_3$	$TiVCrMoC_3T_x$/PVA composite film	High-entropy piezo-electric MXene host in a flexible PVA matrix for self-powered nanogenerators	—	Flexible piezoelectric nanogenerator (PENG); self-powered motion sensor	500 mV and 790 pA at 3.47 N; stable over 1500 cycles; maximum output power = 110.76 pW; finger-motion sensing: ∼85 pA and ∼10 mV	137
$TiVCrMoAlC_3$	$TiVCrMoC_3T_x$	Active HE-MXene for PEC-type photodetectors and saturable absorbers/mode lockers	—	Photodetector (1.0 M KOH) and mode-locked fiber lasers	Response time ≈ 100 fs; $\beta = -0.134$ cm GW^{-1}; modulation depth = 66%; photodetector at 0.4 V: P_{ph} = 1650 nA cm^{-2}, R_{ph} = 35.55 μA W^{-1}, up to 33× $Ti_3C_2T_x$; mode-locked lasers at 1072.5/1553.3/1909.4 nm with SNR 57.4/55.8/54.1 dB	138
$(Ti_{0.21}V_{0.21}Mo_{0.17}Nb_{0.22}Ta_{0.19})_4Al_{0.93}C_3$	$(Ti_{0.21}V_{0.21}Mo_{0.17}Nb_{0.22}Ta_{0.19})_4C_3T_x$	Conductive HE-MXene substrate for anchoring $MoSe_2/Ni_3Se_4$ nanosheets	1350	HER in 0.5 M H_2SO_4 and 1.0 M KOH	Acid: 67 mV @ 10 mA cm^{-2}, 68.7 mV dec^{-1}, C_{dl} = 115.7 mF cm^{-2}. Alkaline: 73 mV @ 10 mA cm^{-2}, 77.8 mV dec^{-1}, C_{dl} = 87.5 mF cm^{-2}. Stable for 24 h in both media	139
$TiVNbMoAlC_3$	$TiVNbMoC_3T_x/Fe_3O_4$	Oxidation-resistant HE-MXene platform for balanced dielectric-magnetic EM-wave absorption	—	EM-wave absorber	HE-MXene/Fe_3O_4-3: $RL_{min} = -57.59$ dB at 1.46 mm; EAB = 4.72 GHz at 1.53 mm; RCS = 1.76 dB m^2; after 30 days, EAB = 4.92 GHz; magnetic saturation ≈ 46 emu g^{-1}	140
$Ti_2V_{0.9}Cr_{0.1}AlC_2$	$Ti_2V_{0.9}Cr_{0.1}C_2T_x$	High-capacitance multi-metal MXene electrode for supercapacitors	1500	Supercapacitor (1 M KOH, three-electrode) and symmetric supercapacitor	553.27 F g^{-1} at 2 mV s^{-1}; 165.51 F g^{-1} at 200 mV s^{-1}; R_{ct} = 8.12 Ω; 90.21% retention after 2000 cycles; device: 20.99 Wh kg^{-1} at 800 W kg^{-1}, 85.18% retention after 2000 cycles	141
$TiVNbMoAlC_3$	$TiVNbMoC_3$ (HE-MXene/G@PP)	Separator mediator and polysulfide regulator	1600	Li–S battery (LiPS capture + Li plating/stripping)	Capacity 654.8/509.4 mAh g^{-1} after 1200 cycles at 1C/2C (0.026/0.031% fade per cycle); Li‖Li symmetric cell stable 6000 h at 40 mA cm^{-2}/40 mAh cm^{-2}	15
$(Ti_{1/5}V_{1/5}Zr_{1/5}Nb_{1/5}Ta_{1/5})_2AlC$	$(Ti_{1/5}V_{1/5}Zr_{1/5}Nb_{1/5}Ta_{1/5})_2CT_x$	Uniform Li deposition and dendrite-free Li metal anodes	1500	Li plating/stripping (symmetric + full cells)	Li nucleation overpotential ≈ 6 mV; symmetric cell 1200 h at 1 mA cm^{-2}, 1 mAh cm^{-2}; deep plating up to 20 mAh cm^{-2}; full cell ≈100 mAh g^{-1} at 10C	29
$Ti_{1.0}V_{0.7}Cr_{0.05}Nb_{1.0}Ta_{1.0}AlC_3$	$Ti_{1.1}V_{0.7}Cr_xNb_{1.0}Ta_{0.6}C_3T_z$	Expand MXene composition space for high-rate supercapacitors	1500	Supercapacitor (1 M H_2SO_4)	490 F g^{-1} and 1688 F cm^{-3} at 2 mV s^{-1}; 89% capacitance retention after 9000 cycles with 99.4% coulombic efficiency at 13.3 A g^{-1}	39
$(TiVCrNbMo)_5AlC_4$	$(TiVCrNbMo)_5C_4T_x$	2D HE-MXene support to build V–Co_2P heterostructure for bifunctional water splitting	—	HER + OER (overall water splitting)	$H_2 : O_2$ ≈ 2 : 1, overall FE ≈ 94.8%	31
$Mo_2Ti_2AlC_3$	CuFeMnCoNi-NC/MXene ($Mo_2Ti_2C_3T_x$)	AEMWE anode catalyst to overcome sluggish OER	900	OER (AEM water electrolyzer, Pt/C cathode)	H_{10} = 267 mV; Tafel 50.9 mV dec^{-1}; 1.91 A cm^{-2} at 2.0 V (70 °C); $\Delta\eta$ ≈ 3 mV after 10 000 cycles	46

Table 1 (*continued*)

HE-MAX	HE-MXene (support/host)	Purpose/role	MAX synthesis temp. (°C)	Reaction/device	Key performance (selected)	Ref.
$TiVNbMoAlC_3$	$TiVNbMoC_3$ (HE-MXene host + interlayer)	Sulfur host and separator-modification layer in Li–S cells	-	Li–S battery sulfur redox + Li plating/stripping regulation	1102.5 mAh g^{-1} at 1C; ≈0.057% decay per cycle over 400 cycles; 4.92 mAh cm^{-2} at 0.2C (5.4 mg cm^{-2}, E/S 8.3 mL mg^{-1})	45
$Ti_{1.0}V_{0.7}Cr_{0.05}Nb_{1.0}0Ta_{1.0}AlC_3$	$Ti_{1.1}V_{0.7}Cr_xNb_{1.0}Ta_{0.6}C_3T_z$	Freestanding HE-MXene films for Zn-ion hybrid capacitors and Li-ion batteries	1500	ZHSC and LIB anodes	ZHSC: 77 mAh g^{-1} at 0.5 A g^{-1}, 43 mAh g^{-1} at 10 A g^{-1}; 87% retention after 10 000 cycles. LIB: 126 mAh g^{-1} at 0.01 A g^{-1}; 48 mAh g^{-1} at 2 A g^{-1}; stable 1000 cycles at 1 A g^{-1}	40
$(Mo_{0.25}Cr_{0.25}Ti_{0.25}V_{0.25})_3AlC_2$	f-$(Mo_{0.25}Cr_{0.25}Ti_{0.25}V_{0.25})_3C_2T_x$	HE-MXene for electro-magnetic (EM) wave absorption	1400–1600	EM absorber (35 wt% composite)	$RL_{min} = -45.0$ dB at 1.52 mm; effective absorption bandwidth (EAB) 5.6 GHz at 1.65 mm	43
$((Mo_{0.2}Cr_{0.2}Nb_{0.2}Ti_{0.2}V_{0.2})_4AlC_3)$	f-$(Mo_{0.2}Cr_{0.2}Nb_{0.2}Ti_{0.2}V_{0.2})_4C_3T_x$				$RL_{min} = -52.8$ dB at 1.58 mm; optimum EAB 3.6 GHz at 1.50 mm	
$TiVNbMoAlC_3$	$TiVNbMoC_3$	To produce conductive, composition-flexible 2D carbides for battery electrodes	1400	LIB anode	Initial 556/1078 mAh g^{-1} (discharge/charge), ICE 51.6%; 725 mAh g^{-1} after 1000 cycles at 1 A g^{-1}	27
$TiVCrMoAlC_3$	$TiVCrMoC_3$			SIB anode	127 mAh g^{-1} after 100 cycles at 100 mA g^{-1} (ICE 44.9%)	
	$TiVCrMoC_3$			LIB anode	127 mAh g^{-1} after 100 cycles at 100 mA g^{-1}	
$(Ti_{1/3}V_{1/3}Nb_{1/3})_2GaC$	$(Ti_{1/3}V_{1/3}Nb_{1/3})_2CT_x$	Fluorine-free synthesis of medium/HE-MXenes for Li-ion storage	1300	LIB anode	≈200 mAh g^{-1} after 300 cycles at 200 mA g^{-1}	47
$(Ti_{1/4}V_{1/4}Nb_{1/4}Ta_{1/4})_2GaC$	$(Ti_{1/4}V_{1/4}Nb_{1/4}Ta_{1/4})_2CT_x$				Li^+ capacity ≈400 mAh g^{-1}; 289 mAh g^{-1} after 300 cycles at 200 mA g^{-1}	
$(Ti_{1/5}V_{1/5}Nb_{1/5}Ta_{1/5}Mo_{1/5})_2GaC$	$(Ti_{1/5}V_{1/5}Nb_{1/5}Ta_{1/5}Mo_{1/5})_2CT_x$				302 mAh g^{-1} after 300 cycles at 200 mA g^{-1}; best high-rate stability among the three	

components that strongly prefer very stable competing carbides or intermetallics.[48] This strategy was explicitly followed in the design of (Ti,V,Cr,Nb,Ta)$_4$AlC$_3$ and TiVNbMoAlC$_3$, where each individual metal forms an M$_4$AlC$_3$-type phase, and the average M/Al/C stoichiometry was tuned to suppress binary carbides.[22,39,48] X-ray diffraction with Rietveld refinement and electron microscopy confirmed that these HE-MAX precursors could be prepared as nearly single-phase materials with only minor secondary phases.[27,39]

Beyond such heuristic selection, thermodynamic screening based on phase-diagram calculations and DFT/CALPHAD approaches is increasingly used to identify promising HE-MAX compositions.[49] Systematic surveys of MAX stability map the formation enthalpy relative to competing phases (ΔH_{cp}) and show that many experimentally realised MAX compounds lie within a narrow window of metastability.[48,50] For multicomponent M sublattices, this analysis is extended by constructing supercell models with random or quasi-random metal distributions and comparing their energies with mixtures of binary carbides, nitrides and intermetallics; cluster-expansion or Monte Carlo methods then capture the impact of short-range order and configurational entropy.[35,48] Such calculations have guided the synthesis of new HE-MAX phases by identifying element sets and stoichiometries for which the high-entropy solid solution is thermodynamically competitive at realistic synthesis temperatures, and by flagging combinations that are likely to decompose.[22,35]

Kinetic factors are equally important because even thermodynamically viable compositions require sufficient diffusion and mixing to form homogeneous solid solutions. Most reported HE-MAX phases have therefore been synthesised by high-temperature reactive sintering of elemental powders or binary carbides, followed by extended dwell times to promote solid-state diffusion. Nemani *et al.*, for example, prepared TiVNbMoAlC$_3$ and TiVCrMoAlC$_3$ by mixing equimolar transition-metal powders with Al and C and sintering at 1600 °C for 4 h under flowing Ar, then converting the resulting HE-MAX phases into multilayer and delaminated HE-MXenes (Fig. 6A).[22] Zhou and co-workers synthesised (Ti,V,Cr,Nb,Ta)$_4$AlC$_3$ by solid-state reaction at 1500 °C for 10 h and showed that deviations from the optimal M/Al/C ratio led to substantial fractions of binary carbides, highlighting the narrow kinetic and compositional window for forming single-phase HE-MAX (Fig. 6B).[39] Mechanical alloying followed by spark plasma sintering (SPS) offers a complementary approach: high-energy ball milling pre-mixes the constituents at the nanoscale, and a subsequent SPS step with rapid heating and applied pressure accelerates densification and diffusion while limiting grain growth, enabling HE-MAX formation from multicomponent powder mixtures.[51] Recently, SPS has been pushed into an

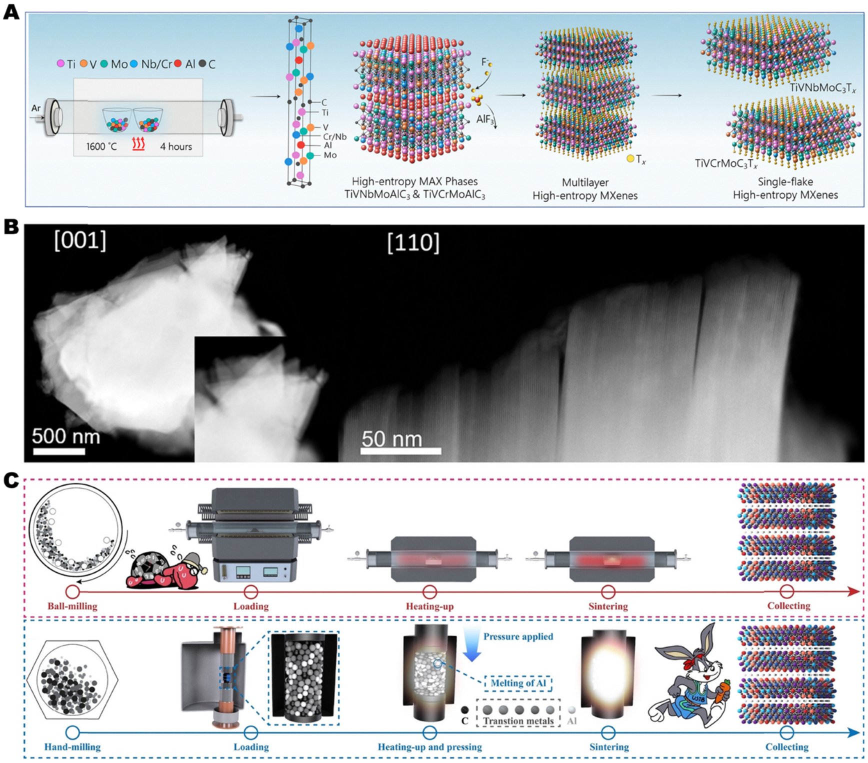

Fig. 6 (A) Reactive sintering route to high-entropy M$_4$AlC$_3$ MAX phases and their subsequent conversion into multilayer and delaminated TiVNbMoC$_3$T$_x$ and TiVCrMoC$_3$T$_x$ HE-MXenes. Reprinted with permission from ref. 22, copyright 2021, American Chemical Society. (B) Representative microstructural characterisation of a 3D HE-MAX phase and its transformation into a 2D HE-MXene, illustrating the importance of composition control for avoiding binary carbide impurities. Reprinted with permission from ref. 39, copyright 2022, American Chemical Society. (C) Comparison between conventional furnace synthesis and an ultra-rapid SPS route, in which transient liquid Al and fast heating enable high-purity HE-MAX formation within minutes. Reprinted with permission from ref. 27, copyright 2024, John Wiley & Sons.

"ultra-rapid" regime, where multicomponent M_4AlC_3-type HE-MAX phases such as $TiVNbMoAlC_3$, $TiVCrMoAlC_3$ and $(Ti_{0.2}V_{0.2}Cr_{0.2}Nb_{0.2}Mo_{0.2})_4AlC_3$ were obtained with $>99\%$ phase purity in only 15 min by using a slight Al overfeed to generate a transient liquid phase that enhances mass transport among the refractory metals (Fig. 6C).[27] While SPS clearly improves kinetic control and densification, it still requires careful optimisation of heating profiles, die materials and atmosphere to avoid contamination, undesired reactions and non-uniform microstructures.

From a practical standpoint, therefore, conventional tube-furnace solid-state reaction, SPS, and (less frequently) hot pressing have emerged as the main platforms for HE-MAX synthesis.[22,27,39] Across all methods, precise control of the M/Al/C (and, where relevant, N) ratios and of the inert atmosphere is critical: small Al excess can assist dissolution of otherwise stable carbides, whereas too much Al leads to persistent intermetallics; similarly, deviations in C content shift the equilibrium towards competing carbides or graphite.[39,48] At the same time, the HE-MAX composition must be chosen with subsequent etching and delamination in mind. Early-transition-metal M_4AlC_3 and M_3AlC_2 phases are generally amenable to selective Al removal in fluoride-containing media, but adding elements that form very stable oxides or non-volatile fluorides can impede etching or cause preferential dissolution. Representative examples of how specific MAX chemistries transform into MXenes under different MAX precursors and etching conditions are summarised in Table 2, which highlights the diversity of precursor structures and etchants in conventional (non-high-entropy) systems.[52–61] Systematic studies on $TiVNbMoAlC_3$, $TiVCrMoAlC_3$ and $(Ti,V,Cr,Nb,Ta)_4AlC_3$ demonstrated that, when the MAX precursor is truly single-phase and the M elements are reasonably etchable, the multicomponent metal distribution is largely retained in the resulting HE-MXenes, with only modest deviations for more reactive species such as Cr.[22,35,39] Thus, robust design of HE-MAX precursors demands an integrated strategy that combines thermodynamic screening (DFT/CALPHAD),[49] elemental selection based on radius and valence compatibility, and kinetic control of synthesis (choice of solid-state reaction, SPS or hot pressing, and precise stoichiometry and atmosphere) to deliver single-phase M_4AlC_3 and M_3AlC_2 structures suitable for conversion into HE-MXenes.

3.2 Etching and delamination of HE-MAX into HE-MXenes

The transformation of HE-MAX phases into their corresponding HE-MXenes follows the same basic principle as for conventional MAX phases: selective removal of the A-layer (typically Al) to generate a layered carbide or nitride that can subsequently be delaminated into few-layer or single-layer flakes. However, the presence of multiple transition metals in HE-MAX phases introduces important additional constraints on etching chemistry, because etching conditions now control not only A-layer removal but also elemental homogeneity within the M-sublattice, defect density in the basal planes and the distribution of surface terminations. Careful selection and optimization of etchants and delamination protocols is therefore central to obtaining phase-pure HE-MXenes with preserved equimolar metal ratios and well-defined surface chemistry for electrocatalysis.[56,62,63]

3.2.1 Adaptation of conventional HF and *in situ* HF etching to high-entropy MAX phases. For high-entropy MAX precursors, the first generation of HE-MXenes has largely been obtained by adapting the classical HF-based routes developed for binary $Ti_3C_2T_x$ and related systems. In these protocols, the A-element layers are removed in concentrated HF while surface terminations (T_x = O, OH, F, occasionally Cl) and intercalated species are introduced in a single step. Chen and co-workers followed this strategy for medium high-entropy M_2GaC (M = Ti, V, Nb, Ta, Mo):[47] direct HF etching produced accordion-like multilayer HE-MXene flakes that could be further combined with graphene-modified polypropylene separators (HE-MXene/G@PP) for Li–S batteries (Fig. 7A).[15] The schematic highlights two features that are directly transferable to other HE-MXene systems relevant for electrocatalysis: (i) the multi-metal M-sublattice is preserved during etching, giving access to fully exposed high-entropy basal planes, and (ii) the interlayer spacing increases upon replacement of Ga by mixed surface terminations, which is beneficial for ion transport and electrolyte access in electrochemical environments.

Given the safety and scalability limitations of concentrated HF, there is growing interest in replacing direct HF with *in situ* HF-forming systems such as NH_4HF_2, NaF/HCl, HBF_4 and $NaBF_4$/HCl. Gentile *et al.* systematically compared $Ti_3C_2T_x$ produced by these agents with material obtained by conventional 5 wt% HF, showing that *in situ* routes can achieve complete A-layer removal, comparable crystallinity

Table 2 Representative MAX precursors, corresponding MXenes and etching chemistries used for MXene synthesis

MAX precursors	MXenes	Etchants	Etching temp.	Ref.
Cr_2TiAlC_2	$Cr_2TiC_2T_x$	Molten NH_4HF_2	180 °C for 40 min	142
Ti_3AlC_2	$Ti_3C_2T_x$	NH_4F	150 °C for 24 h	53
Ti_3AlC_2	$Ti_3C_2T_x$	1 M NH_4HF_2	Room temperature	54
$(Nb_{0.8}Zr_{0.2})_4AlC_3$	$(Nb_{0.8}Zr_{0.2})_4C_3T_x$	LiF + 12 M HCl	50 °C for 168 h	55
Ti_4AlN_3	$Ti_4N_3T_x$	59% KF + 2 9% LiF + 12% NaF	550 °C for 30 min	143
V_2AlC	V_2CT_x	2 g LiF + 40 M HCl	90 °C for 72 h	57
Ti_2AlC	Ti_2CT_x	0.9 M LiF + 6 M HCl	40 °C for 15 h	58
Ti_3AlCN	Ti_3CNT_x	0.66 g LiF + 6 M HCl	30 °C for 12 h	59
Mo_2Ga_2C	Mo_2CT_x	3 M LiF + 12 M HCl	50 °C for 3 h	144
$Hf_3[Al(Si)]_4C_6$	$Hf_3C_2T_x$	35% HF	Room temperature	61

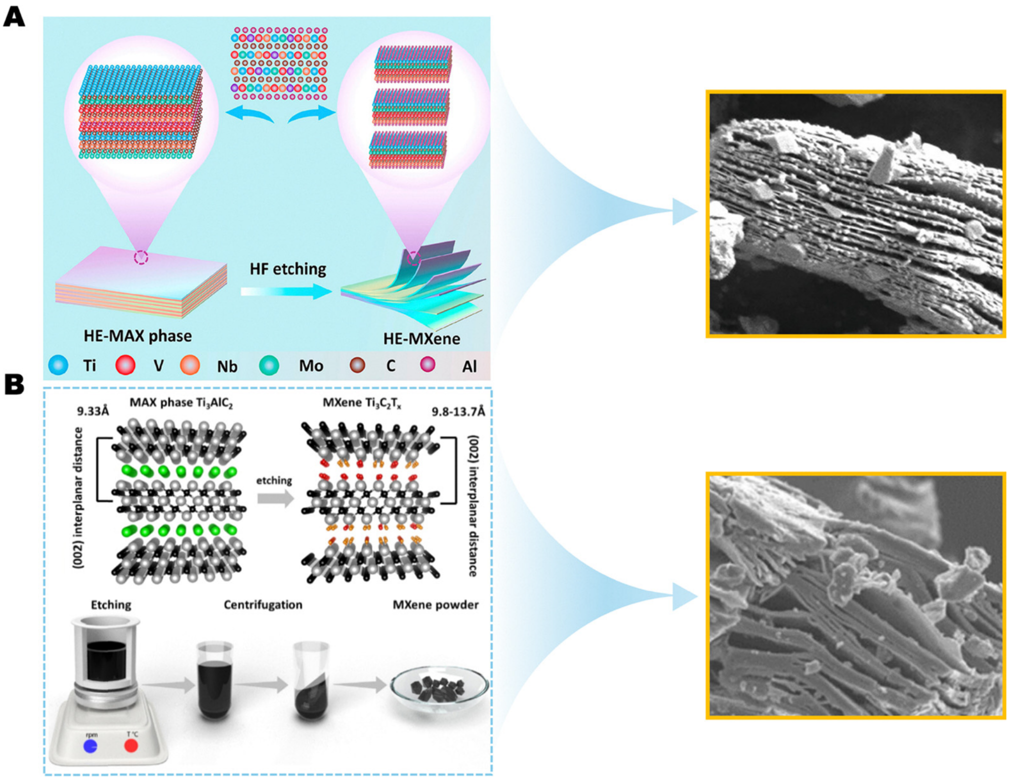

Fig. 7 Conventional and *in situ* HF-based etching routes relevant to HE-MXenes. (A) Direct HF etching of a HE-MAX phase to yield layered HE-MXene flakes that are subsequently incorporated into a HE-MXene/G@PP separator architecture. Reproduced with permission from ref. 15, copyright 2024, American Chemical Society. (B) Structural evolution of Ti_3AlC_2 during etching with *in situ* HF-forming agents to produce $Ti_3C_2T_x$: removal of Al and installation of mixed terminations increase the interlayer distance, while the bottom panel sketches a typical workflow involving etching, washing/centrifugation and recovery of MXene powder. Reproduced with permission from ref. 64, copyright 2022, John Wiley & Sons.

and electrochemical performance while introducing distinct interlayer spacings and intercalated cations (Na^+, NH_4^+, Cl^-) that modulate the MXene structure and charge-storage behaviour.[64] The schematic in Fig. 7B, illustrates how *in situ* HF etching not only replaces Al with mixed terminations but also expands the (002) spacing and yields stacked MXene platelets suitable for further delamination. Translating these insights to HE-MAX systems implies that etchant choice must be optimised not only for complete and composition-preserving A-layer removal, but also for controlled introduction of terminations and interlayer species that favour the targeted electrocatalytic reaction while reducing the reliance on highly hazardous HF.[64] These conventional and *in situ* HF approaches provide the baseline chemistry from which more sustainable, termination-engineered etching protocols for HE-MXenes will be developed in later sections.

3.2.2 Emerging etching strategies: molten salts, halide-hydrothermal and supercritical CO_2.

Beyond HF-based and *in situ* HF routes, several alternative etching strategies originally developed for conventional MXenes offer attractive opportunities for HE-MXenes, particularly when control over terminations, oxidation stability and scalability are critical for electrocatalysis. Lewis-acidic molten-salt etching uses molten halide salts such as $CuCl_2$/NaCl/KCl, $ZnCl_2$ or $NiCl_2$ to remove the A layer through high-temperature redox or displacement reactions, typically producing MXenes with halide (–Cl, –Br) terminations and reduced oxygen content.[38,50,63,65] Such MXenes often display slower oxidation kinetics than acid-etched analogues, which is beneficial for long-term electrochemical operation.[65] Wang *et al.* illustrated the electrocatalytic potential of this approach by synthesizing Pt–M@$Ti_3C_2T_x$ (M = Fe, Co, Ni, Cu, Zn) in a single molten-salt step, yielding MXene-supported multimetal nanoparticles with tailored surface terminations and high HER activity (Fig. 8A and B).[66] For HE-MAX phases, analogous Lewis-acidic media could provide finer control over halide terminations and more homogeneous etching across multiple metals, although possible selective reduction or segregation of specific elements must be carefully assessed.[38]

Halide-mediated hydrothermal etching represents a complementary fluoride-free strategy. In this case, concentrated halide solutions (*e.g.* Cl^-, Br^-, I^-) at elevated temperature promote A-layer dissolution and introduce halogen-rich terminations without using HF.[7] Xu *et al.* recently demonstrated a halogen-ion-mediated hydrothermal route that enables gram- to tens-of-gram-scale synthesis of diverse MXenes, including Mo_2CT_x, with controllable morphology and termination chemistry (Fig. 8C and D).[67] Compared with classical alkali-hydrothermal and electrochemical protocols,[7] this approach combines safer processing with explicit control over the halide content of the surface, features that are

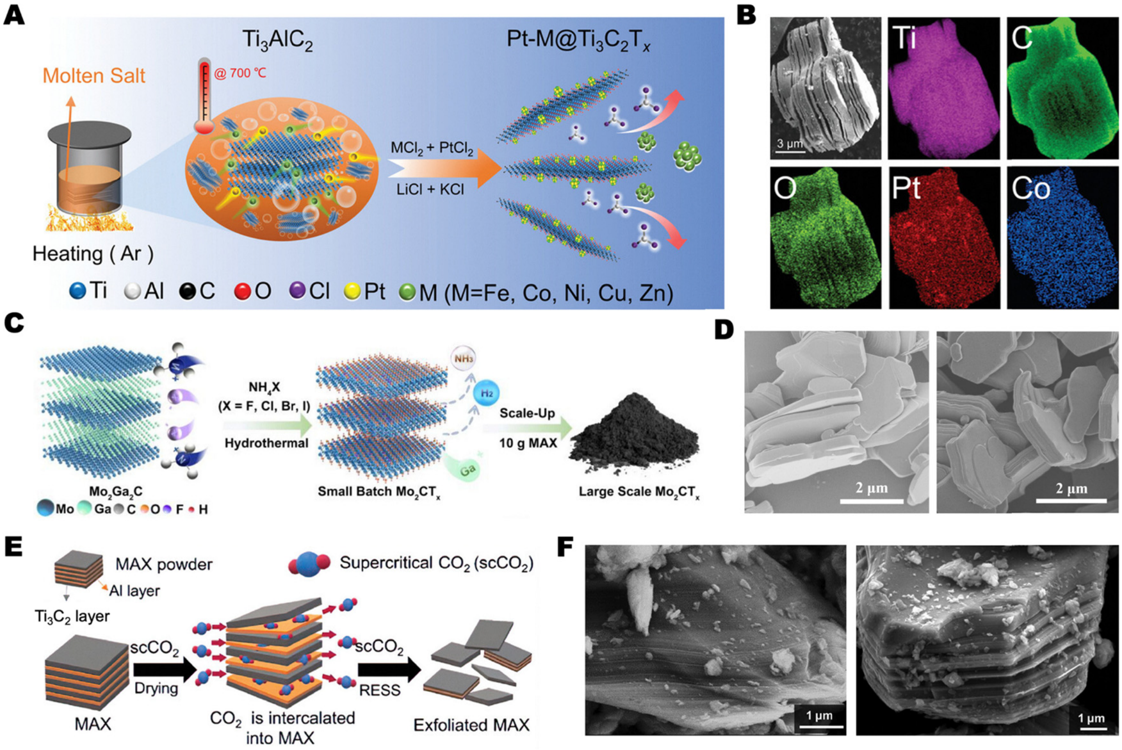

Fig. 8 Emerging etching and exfoliation strategies relevant to HE-MXenes. (A) Molten-salt synthesis of Pt–M@$Ti_3C_2T_x$. (B) SEM and EDS maps of Pt–Co@$Ti_3C_2T_x$. Reprinted with permission from ref. 66, copyright 2023, John Wiley & Sons. (C) Halogen-ion-mediated hydrothermal synthesis of Mo_2CT_x. (D) SEM images showing morphology retention on scale-up. Reprinted with permission from ref. 67, copyright 2025, John Wiley & Sons. (E) $scCO_2$-assisted exfoliation scheme. (F) SEM images of pristine and exfoliated samples. Reprinted with permission from ref. 68, copyright 2024, John Wiley & Sons.

particularly attractive for HE-MXenes where subtle changes in terminations can strongly modulate multi-metal active sites.

Supercritical CO_2 ($scCO_2$)-assisted etching and exfoliation is an emerging technique designed to overcome diffusion limitations and throughput constraints of purely liquid-phase methods. Kim *et al.* showed that $scCO_2$, combined with suitable etchants, can intercalate and delaminate Ti_3AlC_2, producing few-layer MXene nanosheets without harsh acids or bases and with improved control over layer spacing (Fig. 8E and F).[68] In this process, $scCO_2$ enhances transport of etchant species into the MAX structure, facilitates removal of by-products and enables continuous, scalable processing.[7] Extending $scCO_2$-assisted strategies to HE-MAX phases could substantially increase the practical availability of HE-MXenes and allow simultaneous tuning of termination composition and interlayer structure, provided that the phase stability of multicomponent carbides under supercritical conditions is confirmed experimentally. Overall, molten-salt, halide-hydrothermal and $scCO_2$-assisted routes expand the toolbox for tailoring defect density, termination chemistry and oxidation resistance beyond what is accessible with HF-based methods. For HE-MXenes, in which the interplay of multiple metals and terminations underpins their emerging electrocatalytic potential, rational adaptation and combination of these etching strategies will be essential.

3.2.3 Delamination strategies and their impact on flake morphology.

After selective A-site removal, multilayer HE-MXenes must be delaminated into few-layer or single-layer flakes to expose active basal planes and enable uniform electrode architectures. In principle, HE-MXenes can be delaminated by the same families of methods developed for conventional MXenes, but their multimetal chemistry makes control over flake size, defect density and oxidation particularly important. Early HE-MXene films from $Ti_{1.1}V_{0.7}Cr_xNb_{1.0}Ta_{0.6}C_3T_z$ were obtained by tetrabutylammonium hydroxide (TBAOH) intercalation of HF-etched powders, followed by mild sonication to separate ultrathin flakes.[40] Organic bases such as TBAOH and TMAOH are effective intercalants for many $Ti_3C_2T_x$-type MXenes and remain viable for HE-MXenes, but they introduce residual species and can fragment flakes if sonication is too vigorous.[65,69] Inorganic bases (for example NaOH) and small-cation intercalation using Li^+, Na^+ or K^+ salts provide cleaner delamination with larger lateral sizes, although the resulting flakes are often thicker and the efficacy can depend sensitively on termination chemistry.[69–71] Electrochemical delamination, in which cations are driven between layers under an applied potential, offers an alternative route that can be combined with fluoride-free etching and can yield MXenes with controlled terminations, but must be tuned to avoid overoxidation or preferential leaching of specific metals in HE-MXenes.[7,72,73]

A complementary direction is purely mechanical or hydrodynamic delamination without chemical intercalants, which directly targets scalable production and preservation of flake integrity. Inman *et al.* showed that multilayer $Ti_3C_2T_x$ can be efficiently delaminated by passing concentrated slurries through a three-roll mill, where high shear at the roll gaps peels off single- and few-layer flakes with capacitances comparable to LiCl-delaminated MXene (Fig. 9A).[74] High-pressure homogenisation (HPH) extends this concept by combining shear, cavitation and impact forces in a flow-through geometry: ml-MXene is driven through a small orifice into a larger reactor volume, generating cavitation bubbles that nucleate and collapse along the basal planes, leading to delaminated MXene with high yield and throughput and without Li^+ or bulky organic intercalants (Fig. 9B).[74] In a related shear-stress-induced delamination (SSID) strategy, Zhou *et al.* used a pan-mill-type wet grinder to subject m-$Ti_3C_2T_x$ to intense hydrodynamic shear between rotating and stationary discs.[75] Compared with manual handshaking, ultrasonication and ball milling (Fig. 9C), the SSID process (Fig. 9D and E) generated few-layer flakes (G-MXene) with larger lateral size, fewer defects and lower oxidation, which translated into higher film conductivity and better mechanical integrity.[75]

For HE-MXenes, these observations highlight several design principles. First, delamination routes that minimise flake fragmentation and edge oxidation, such as soft organic-base intercalation, HPH, or SSID-type shear grinding, are preferable because catalytic activity and electronic transport depend strongly on lateral size and structural integrity.[65,74–76] Second, any method employing strong bases, cavitation or impact must be examined for its influence on multimetal stoichiometry and local terminations, since preferential oxidation or dissolution of one component could erode the intended high-entropy chemistry. Finally, because practical electrocatalytic devices will require gram- to kilogram-scale quantities of HE-MXenes, scalable mechanical schemes such as HPH and SSID, potentially combined with mild intercalation, are especially attractive for translating the emerging promise of HE-MXenes in electrocatalysis from laboratory studies to larger-scale applications.

3.2.4 HE-specific considerations: compositional integrity, defects and terminations. In multicomponent HE-MXenes, etching and delamination directly determine how the high-entropy metal sublattice is expressed at the atomic scale, by controlling vacancy populations and termination chemistry rather than simply removing the A-layer. Work on monometallic $Ti_3C_2T_x$ already illustrates how sensitive this balance is. In single-layer $Ti_3C_2T_x$, atomic-resolution HAADF-STEM combined with DFT shows that Ti vacancies form both as isolated VTi and as vacancy clusters, with formation energies that decrease as cluster size increases; increasing HF concentration drives a higher density of VTi and larger clusters, and the overall defect population scales systematically with etching conditions (Fig. 10A and B).[77] These results indicate that fluoride etching simultaneously generates functional terminations and a

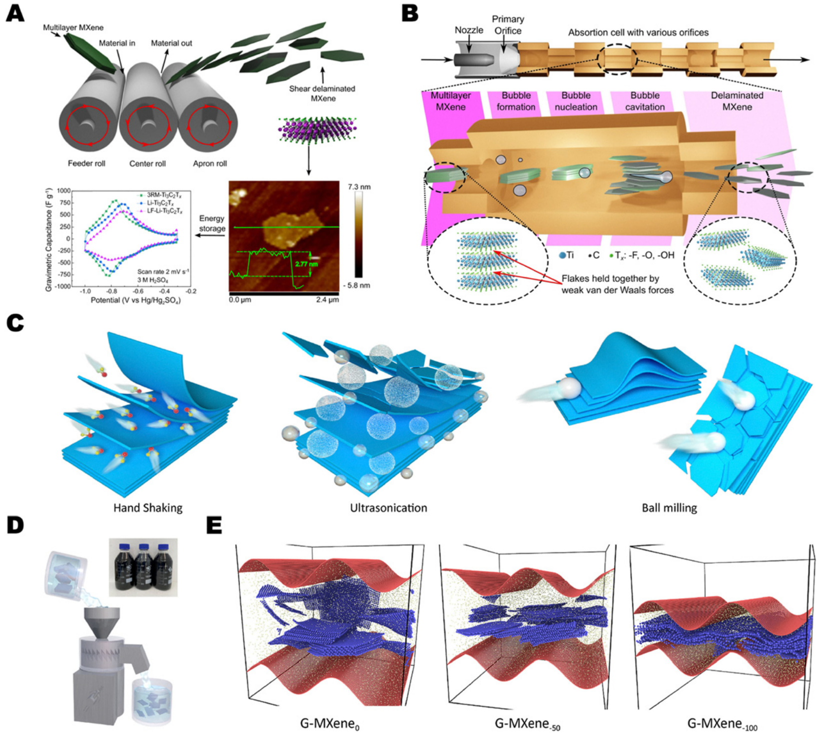

Fig. 9 Delamination strategies and their influence on MXene flake morphology. (A) Shear-delamination of multilayer MXene using a three-roll mill. Reprinted with permission from ref. 76, copyright 2022, Springer Nature. (B) High-pressure homogeniser processing of multilayer MXene, where flow constriction and cavitation drive intercalant-free delamination. Reprinted with permission from ref. 74, copyright 2023, Elsevier. (C) Comparison of mechanical delamination routes: hand shaking, ultrasonication and ball milling. (D) Shear-stress-induced delamination in a pan-mill-type wet grinder. (E) Molecular-dynamics depiction of G-MXene delamination and dispersion during SSID. Reprinted with permission from ref. 75, copyright 2023, Elsevier.

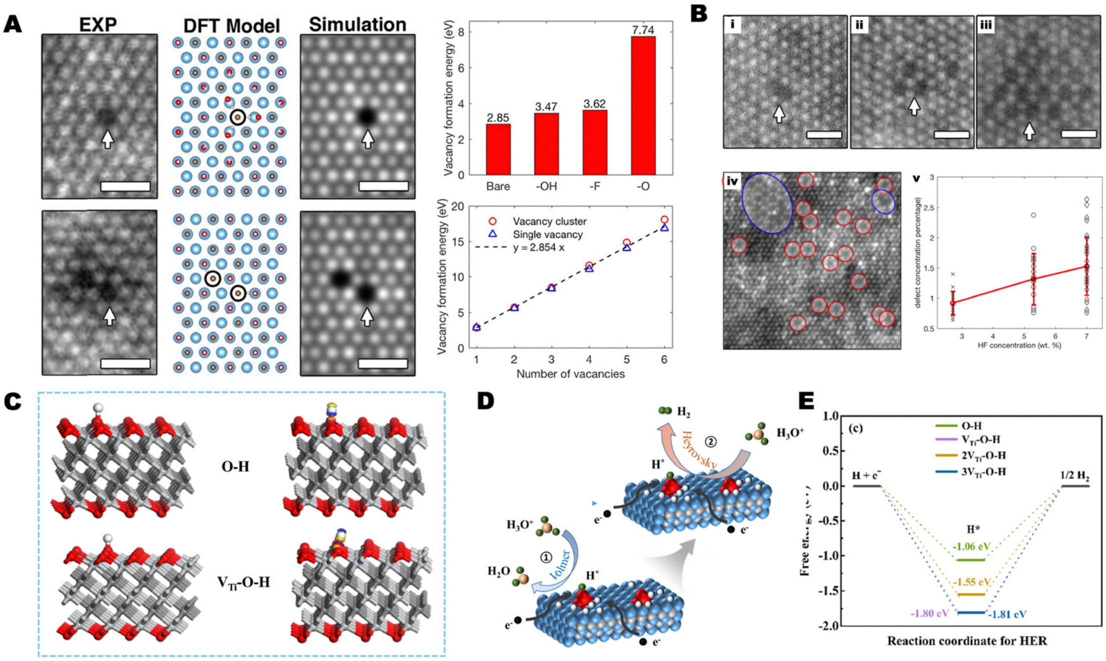

Fig. 10 Defect and termination control during etching and its implications for MXene-based HER electrocatalysts. (A) and (B) Atomic-resolution HAADF-STEM images and statistics of Ti vacancies and vacancy clusters in monolayer $Ti_3C_2T_x$ prepared with different HF concentrations, showing increased defect clustering with stronger etching. Reprinted with permission from ref. 77, copyright 2016, American Chemical Society. (C) DFT models of H adsorption on pristine $Ti_3C_2T_x$, Ti-vacancy-rich $Ti_3C_2T_x$, and Pt anchored at Ti-vacancy sites. (D) Schematic HER pathway on Pt@$Ti_3C_2T_x$ in acidic media. (E) Calculated HER free-energy diagrams showing that Pt–VTi sites provide the most favourable ΔG_{H*}. Reprinted with permission from ref. 78, copyright 2025, Elsevier.

hierarchy of metal vacancies, and that both must be treated as controllable parameters rather than side-effects of synthesis.

Building on this, Yang *et al.* engineered Ti-vacancy-rich $Ti_3C_2T_x$ as a support for ultra-low-loading Pt, using HF etching time to tune VTi concentration and then anchoring Pt by photodeposition.[78] DFT models show that H adsorption on pristine $Ti_3C_2T_x$, on vacancy-rich $Ti_3C_2T_x$ with O terminations, and on Pt anchored at VTi sites leads to distinct charge distributions and hydrogen adsorption free energies (Fig. 10C and E); Pt occupying Ti-vacancy sites gives $\Delta G_{H*} \approx -0.38$ eV, much closer to thermoneutral than on vacancy-free or vacancy-only surfaces, and is associated with enhanced electronic density of states near the Fermi level and improved charge transport. The corresponding schematic HER pathway for PMX-24 in acidic media (Fig. 10D) highlights how Ti vacancies act as specific anchoring sites that stabilise atomically dispersed Pt and maintain high mass activity at ultralow loading.

For HE-MXenes, these case studies imply that an "appropriate" etching and delamination protocol must do more than yield exfoliated flakes. It should (i) retain the near-equimolar metal distribution of the parent HE-MAX while avoiding preferential dissolution of more labile elements, (ii) generate a controlled, moderate density of metal vacancies and vacancy clusters that can act as active sites or anchoring sites without compromising conductivity, and (iii) produce termination ensembles (O/OH, F, Cl/Br, *etc.*) that are compatible with the targeted electrocatalytic reaction. Because different metals in a HE-MXene are likely to have different vacancy formation energies and affinities for specific terminations, small changes in HF concentration, etching time or post-treatment can translate into non-uniform local chemistries that alter adsorption energetics. At present, etching and post-treatments mainly controlled termination chemistry at the ensemble level (overall –O/–OH/–F/–Cl ratios) rather than enabling site-specific placement of a given termination above a selected metal atom. Consequently, differences in metal–termination affinities could translate into batch-to-batch variability unless processing histories and termination compositions are carefully standardised and quantified. Systematic comparison of HF and *in situ* HF etching, molten-salt and alkali-assisted routes, together with carefully chosen delamination strategies, therefore needs to be coupled with atomic-scale characterisation (AC-HAADF-STEM, XPS, EPR, ICP) to map how processing histories reshape defect and termination landscapes.[77,78] In the context of high-entropy electrocatalysis, controlling these landscapes is central to preserving compositional integrity while deliberately creating the ensembles of active sites that underpin the performance gains discussed in later sections.

3.3 Structural and chemical characterization

Establishing that a material is a genuine HE-MXene, rather than a mixture of phases or a partially etched laminate, requires complementary diffraction, microscopy and spectroscopy (Fig. 11). At the average-structure level, powder XRD with Rietveld refinement is used to confirm that HE-MAX precursors are single-phase and to track their transformation into

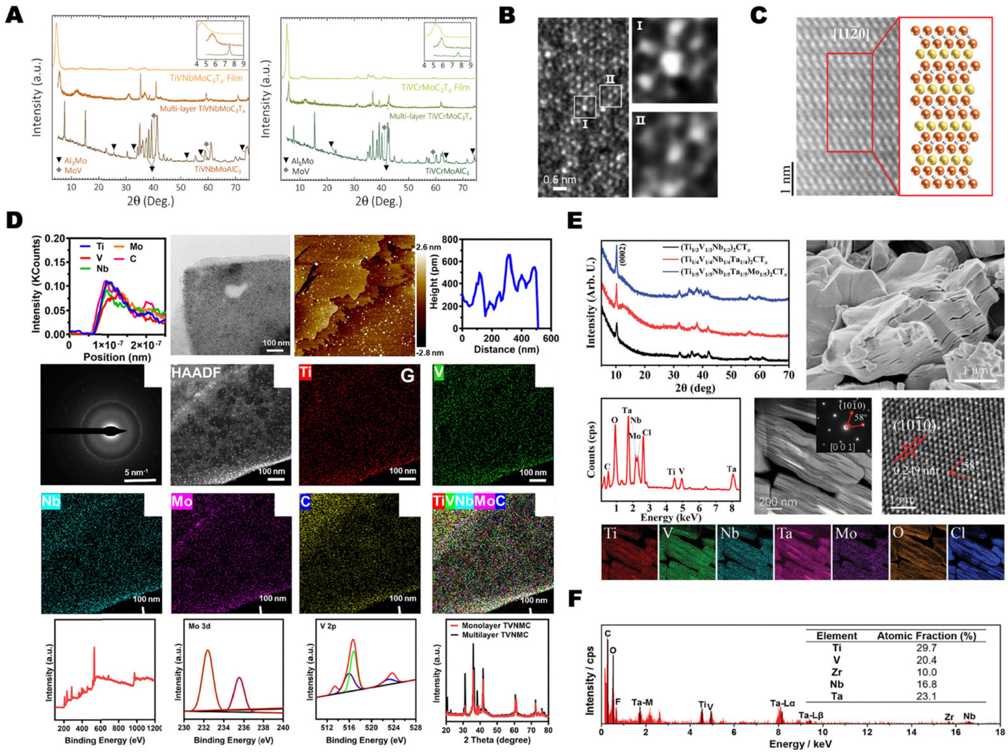

Fig. 11 Structural and chemical characterisation of representative HE-MXenes. (A) XRD patterns of TiVNbMoAlC$_3$ and TiVCrMoAlC$_3$ HE-MAX phases and their corresponding HE-MXenes, showing phase evolution and the low-angle shift/broadening of the (002) peak after etching/delamination. Reprinted with permission from ref. 22, copyright 2021, American Chemical Society. (B) Atomic-resolution HAADF-STEM image of TiVNbMoC$_3$T$_x$ showing multi-metal occupation and lattice distortion. Reprinted with permission from ref. 29, copyright 2021, John Wiley & Sons. (C) Aberration-corrected HAADF-STEM image of (Ti,V,Zr,Nb,Ta)$_2$CT$_x$ illustrating the layered structure and local distortion. Reprinted with permission from ref. 47, copyright 2023, John Wiley & Sons. (D) TEM, AFM, SAED, HAADF-STEM/EDS, XPS and XRD analyses of monolayer TVNMC HE-MXenes confirming single-layer thickness and uniform elemental distribution. Reprinted with permission from ref. 16, copyright 2025, Elsevier. (E) XRD, morphology and elemental mapping of Ga-containing (Ti,V,Nb,Ta,Mo)$_2$CT$_x$ MXenes prepared by Lewis-acid molten-salt etching, showing phase purity, accordion-like morphology and homogeneous multi-metal distribution. Reprinted with permission from ref. 47, copyright 2023, John Wiley & Sons. (F) Representative EDS spectrum of (Ti,V,Zr,Nb,Ta)$_2$CT$_x$ confirming near-equimolar metal mixing on the M-sublattice. Reprinted with permission from ref. 29, copyright 2021, John Wiley & Sons.

HE-MXenes. For TiVNbMoAlC$_3$ and TiVCrMoAlC$_3$, Nemani *et al.* showed that both the MAX and MXene stages display single sets of reflections consistent with M$_4$AlC$_3$ and M$_4$C$_3$ stacking, with progressive broadening and low-angle shifts of the (002) peak on going from MAX to multilayer and then delaminated films (Fig. 11A).[22] Similar XRD signatures, single-phase M$_2$AX patterns and expanded (000ℓ) reflections after etching have been reported for Ga-containing medium/high-entropy (Ti,V,Nb,Ta,Mo)$_2$CT$_x$ and related systems, underlining that high-entropy mixing can be realised in both M$_4$X$_3$- and M$_2$X-type MXenes.[16,47]

Local chemical disorder and lattice distortion, which are central to high-entropy behaviour, must be resolved by high-resolution electron microscopy. STEM-HAADF imaging of TiVNbMoC$_3$T$_x$ reveals atomic columns with varying intensities arranged in a distorted hexagonal lattice, consistent with multi-metal occupation of the M-sublattice (Fig. 11B).[29] Du *et al.* observed analogous contrast fluctuations and non-ideal M–X–M angles in (Ti,V,Zr,Nb,Ta)$_2$CT$_x$, directly visualising the strain field associated with multi-principal-element mixing (Fig. 11B and F).[29] More recently, monolayer TVNMC HE-MXenes have been characterised by a combination of TEM, SAED, AFM and atomic-resolution HAADF-STEM/EDS, demonstrating single-layer morphology, uniform Ti/V/Nb/Mo/C distributions and Vegard-like shifts in diffraction peaks relative to binary analogues (Fig. 11D).[16] Together, these studies show that genuine HE-MXenes exhibit both long-range layered order and nanoscale chemical disorder without detectable metal clustering.

Spectroscopic probes then establish oxidation states, termination chemistry and element-specific local environments. XPS survey and high-resolution spectra provide the relative amounts of C, N, O, F, Cl and other anions, deconvolve M–C, M–N, M–O and M–Cl/F contributions and verify near-equimolar metal ratios through depth-profiling.[22,42,46,77,78] In HE-MXenes such as (Ti,V,Zr,Nb,Ta)$_2$CT$_x$ and Ga-derived (Ti,V,Nb,Ta,Mo)$_2$CT$_x$, the coexistence of multiple oxidation states and mixed –O/–Cl (or –F/–O) terminations has been correlated with the high density of distinct adsorption sites inferred from electrochemical measurements.[29,47] Element-selective X-ray absorption spectroscopy (XANES/EXAFS) further refines this picture by resolving coordination numbers, bond lengths and disorder parameters separately for each metal, allowing short-range order and local electronic structure to be quantified in truly multicomponent lattices.[35,79]

For electrocatalysis, static *ex situ* characterisation is insufficient: structural and chemical evolution under potential must also be monitored. *Operando* Raman and XAS have begun to reveal termination rearrangements, oxidation-state changes and possible reconstruction of HE-MXene surfaces during HER, OER and related reactions, while electrochemical impedance spectroscopy links flake restacking, defect density and termination composition to charge-transfer resistance and ion transport.[80,81] Careful integration of these *operando* tools with the *ex situ* methods summarised above is therefore essential to build reliable composition–structure–function relationships and to substantiate the claimed high-entropy advantages of HE-MXenes in sustainable electrocatalysis.[22,38]

4. Electronic structure, active sites and theoretical modelling

4.1 Electronic structure and lattice distortion in high-entropy MXenes

Substituting several transition metals on the M-sublattice profoundly modifies the electronic structure of MXenes relative to mono-metal systems such as $Ti_3C_2T_x$ or Mo_2CT_x. In single-metal MXenes, states near the Fermi level originate from a narrow set of M-d orbitals, giving a relatively well-defined d-band centre and a limited spread of adsorption energies for surface intermediates. In contrast, HE-MXenes such as $TiVNbMoC_3T_x$ or $(Ti,V,Zr,Nb,Ta)_2CT_x$ feature multiple d-manifolds with slightly different energies and occupancies, producing broadened projected densities of states and locally varying metal–C/T bond strengths (Fig. 12A). High-throughput DFT calculations on $TiVNbMoC_3$ and $TiVCrMoC_3$ have shown that distinct local metal ensembles give rise to a wide distribution of local d-band centres and crystal-orbital Hamilton populations for M–C and M–T bonds, in sharp contrast to the electronically more uniform $Ti_3C_2T_x$.[82] Charge-transfer analyses indicate partial electron donation from more electropositive metals (*e.g.* Zr, Nb) to more electronegative neighbours (*e.g.* V, Mo, Ta), which adjusts the occupation of antibonding d states and further diversifies the local electronic environments.

This electronic heterogeneity translates directly into continuous distributions of adsorption energies for electrocatalytic intermediates. On MXene basal planes, intermediates may adsorb on on-top M sites or on multi-metal bridge/hollow motifs coordinated by two or three neighbouring surface metal atoms; in HE-MXenes these can be viewed as bi-/tri-metal ensemble sites whose atomic identities vary statistically across the surface. Therefore, the ''continuous'' adsorption-energy distribution arose from the local ensemble geometry/composition of the coordinating metals (*e.g.*, a given bridge/hollow

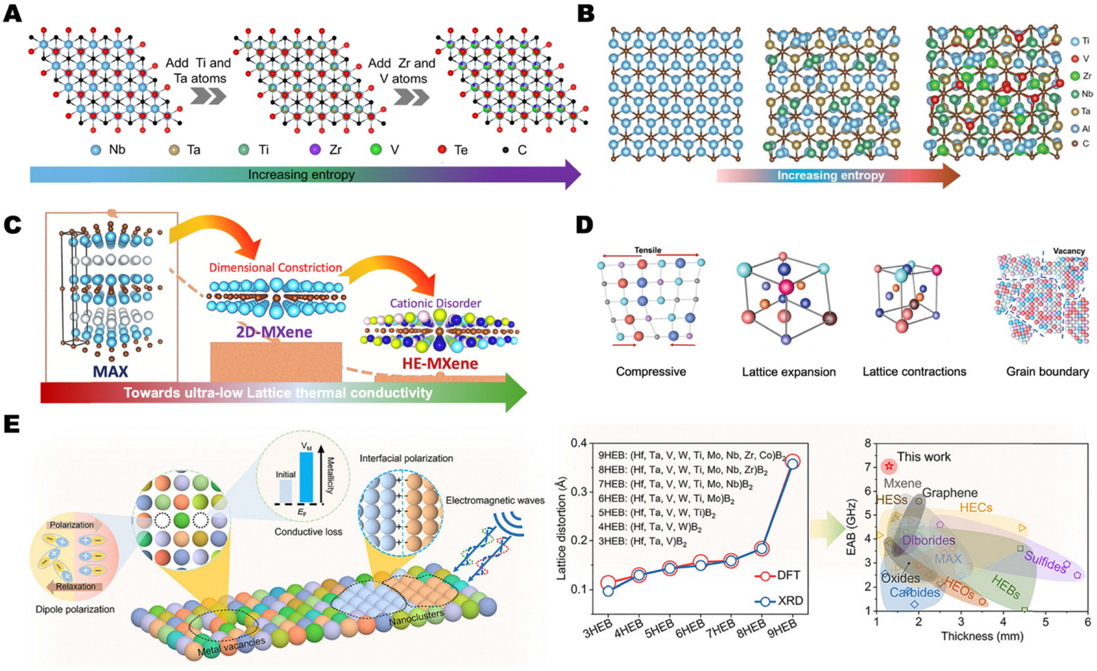

Fig. 12 Electronic structure and lattice distortion in HE-MXenes and related HEMs. (A) Evolution of MXene lattices from ordered to high-entropy configurations as the number of metals on the M-sublattice increases. Reprinted with permission from ref. 82, copyright 2025, Springer Nature. (B) Schematic of lattice distortion in high-entropy MAX/MX phases caused by random multi-metal occupancy. Reprinted with permission from ref. 29, copyright 2021, John Wiley & Sons. (C) Phonon-transport engineering in HE-MXenes, where cation disorder enhances phonon scattering and lowers lattice thermal conductivity. Reproduced with permission from ref. 86, copyright 2024, Elsevier. (D) Local strain, lattice expansion/contraction, and defect formation in heavily distorted high-entropy lattices. Reproduced with permission from ref. 87, copyright 2025, John Wiley & Sons. (E) Lattice-distortion engineering in high-entropy diborides, showing the role of vacancies and nanoclusters in tuning electrical and interfacial properties. Reproduced with permission from ref. 88, copyright 2025, Elsevier.

motif) and its corresponding site-specific electronic structure, which can be captured by a local d-band centre (or related bond-strength descriptor) rather than a single global d-band centre for the entire surface. In practice, intermediates did not converge on one universal "tri-metal bridge site"; instead, the preferred motif depended on the adsorbate and termination environment, while the binding strength within a given motif scaled with the local electronic descriptor. For HE-MXenes, DFT studies on O-terminated $TiVNbMoC_3$ found that the hydrogen adsorption free energy, ΔG_{H^*}, spans a broad range across different surface sites, with a significant fraction of configurations having near-optimal ΔG_{H^*} values close to zero, thereby rationalising improved HER activity compared with simpler carbides.[82] A systematic survey of HE $M_2C(T)_2$ MXenes (M = Ti, V, Nb, Mo, Ta; T = O, OH, F) further demonstrated quasi-continuous ΔG_{H^*} distributions arising from random metal and termination arrangements; importantly, each composition statistically contains a subset of sites with ΔG_{H^*} in the optimum ± 0.1–0.2 eV window even when the average binding is suboptimal.[18] Similar ensemble effects have been predicted and, in related HEMs, observed for *O, *CO and $*N_2H_x$ intermediates, suggesting that HE-MXenes can host dense landscapes of near-optimal sites for multi-step reactions such as OER/ORR, CO_2RR and NRR.[83–85]

Electronic complexity is intimately linked to lattice distortion. Random occupancy of metals with different radii and bonding preferences generates local compressive and tensile regions, deviations from ideal hexagonal symmetry and non-uniform interatomic distances in both HE-MAX precursors and their MXene derivatives (Fig. 12B).[29] In $(Ti,V,Zr,Nb,Ta)_2CT_x$, atomic-resolution STEM has directly visualised such distortions, while phonon-transport calculations on model HE-MXenes show that cation disorder introduces strong static strain fields and intensive phonon scattering, driving the lattice thermal conductivity to values far below those of single-metal analogues (Fig. 12C).[86] More generally, entropy-engineered 2D materials and high-entropy ceramics exhibit strain-induced lattice expansion/contraction, grain-boundary formation and vacancy generation (Fig. 12D), which modulate bond lengths, local symmetry and charge density around active sites.[29,87] Recent work on high-entropy diborides further illustrates how lattice distortion, metal vacancies and chemical nanoclusters cooperate to enhance charge transport and interfacial polarization (Fig. 12E), providing a broader framework for understanding how distortion-controlled local fields and defect landscapes can be exploited in high-entropy systems.[88] Taken together, HE-MXenes should be viewed as electronically and mechanically heterogeneous 2D carbides/carbonitrides in which broadened, compositionally tunable d-bands coexist with disorder-induced strain and defect fields. This combination naturally generates statistical ensembles of adsorption sites with a continuum of binding energies and dynamic response to external fields, which underpins their potential as platform electrocatalysts for complex, multi-electron energy-conversion reactions.

4.2 Surface terminations and defect chemistry

In MXenes, and even more so in HE-MXenes, surface terminations are part of the crystal structure rather than incidental functional groups. The composition and arrangement of –O, –OH, –F, –Cl and other terminations are set by the etching route and subsequent treatments,[7,42,89] but their thermodynamic role is now better quantified. High-throughput DFT screening across 29 transition metals, four layer thicknesses (n = 1–4) and eleven terminations showed that the energy above the convex hull, ΔE_{hull}, is governed at least as strongly by the terminating species as by the underlying metal carbide or nitride (Fig. 13A–C).[90] Large regions of the $M_{n+1}X_nT_2$ design space are predicted to be thermodynamically stable or metastable only for specific terminations (in particular O- and F-based groups), while other terminations stabilise only narrow subsets of compositions. This map is directly relevant to HE-MXenes: any attempt to combine multi-principal M-sublattices with unconventional terminations must respect these stability windows or rely on electrochemical environments that can kinetically stabilise metastable surfaces.

For electrocatalysis, these terminations regulate not only stability but also the distribution of adsorption energies and interfacial properties. Existing experimental and computational studies on mono- and double-transition-metal MXenes have already shown that O-rich surfaces generally strengthen binding of H*, O* and OOH*, often pushing HER or OER activity towards the top of volcano plots, whereas F-rich surfaces tend to weaken adsorption and can suppress CO_2 activation.[89–93] In HE-MXenes, this termination dependence is superimposed on the compositional heterogeneity of the M-sublattice: the same –O or –OH group can experience very different local electronics depending on whether it is coordinated to, for example, Ti–V–Nb triplets or Mo–Ta–Zr ensembles. For sustainable energy conversion, a key design target is to control terminations and local active-site environments. Recent DFT work on multi-metal $M_2C(T)_2$ MXenes indicates that the distribution of hydrogen adsorption free energies ΔG_{H^*} depends jointly on termination identity and the underlying metal cluster.[18] Importantly, current top-down synthesis routes (etching followed by washing/intercalation and optional post-treatments) did not enable deterministic, site-specific regulation of terminations on a metal-by-metal basis; instead, terminations populated surface sites statistically, with possible local preferences dictated by the metal identity and local coordination environment. This implied that HE-MXene surfaces should be described by joint distributions of metal-neighbourhood motifs and termination species, and it also raised the possibility of batch-to-batch differences in activity/stability if termination ratios and post-treatment histories varied between preparations. Accordingly, we emphasised the need to report etching/post-treatment conditions and to quantify termination composition (*e.g.*, by XPS depth profiling and complementary surface-sensitive analyses) when comparing HE-MXenes across studies. Implying that mixed terminations on HE-MXenes generate a dense spectrum of adsorption sites, some of which naturally fall near optimal binding energies for HER and for the suppression of competing reactions. For sustainable energy conversion, a key design target is therefore not a single ideal termination, but a statistically favourable mixture of terminations and metal

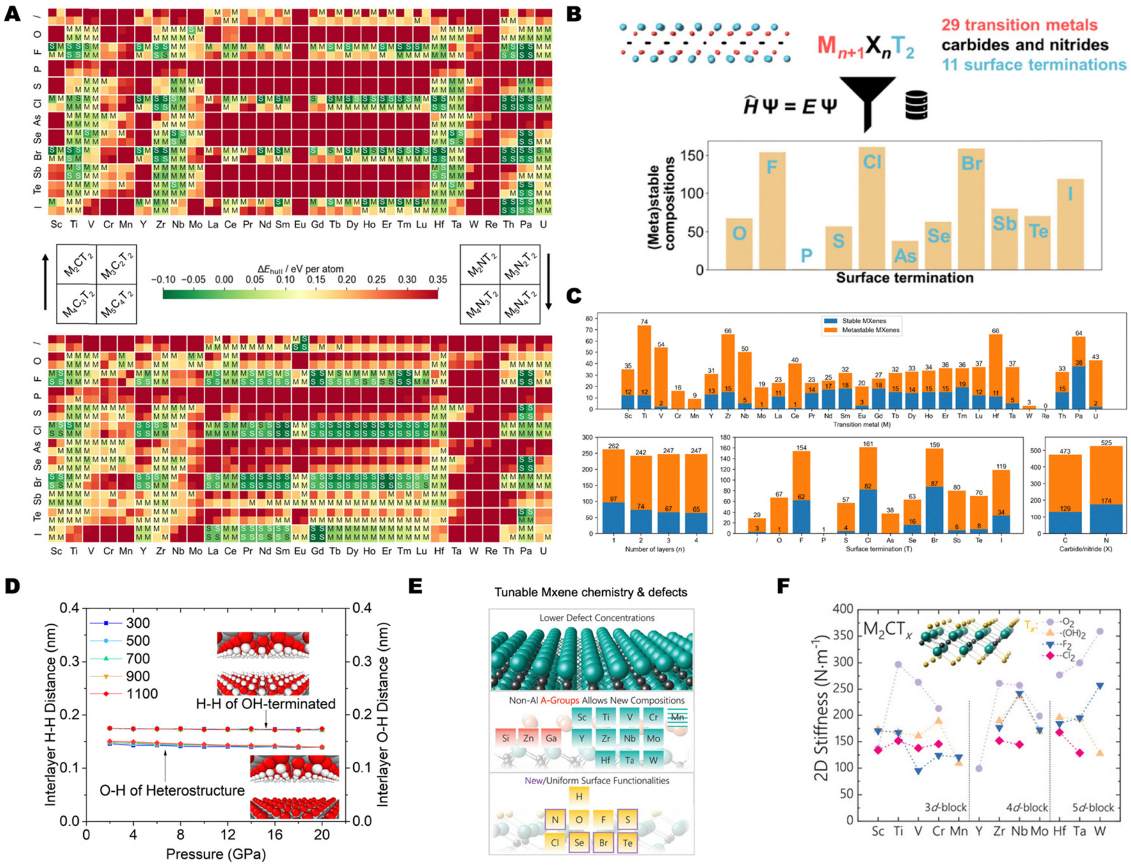

Fig. 13 Termination- and defect-dependent stability and mechanical behaviour of MXenes and implications for HE-MXenes. (A) High-throughput DFT heat map of the thermodynamic stability of $M_{n+1}X_nT_2$ compositions across transition metals and terminations. (B) Computational screening workflow and the number of stable/metastable compositions for different terminations. (C) Statistics of stable and metastable MXenes as a function of metal, layer number, termination, and carbide/nitride chemistry. Reprinted with permission from ref. 90, copyright 2024, American Chemical Society. (D) Pressure-dependent interlayer distances in OH-terminated MXenes and MXene heterostructures, illustrating the role of hydrogen-bonded terminations in structural response. Reprinted with permission from ref. 98, copyright 2023, Springer Nature. (E) Schematic of tunable MXene chemistry and defects enabled by different etching strategies. (F) Calculated 2D stiffness of M_2CT_x monolayers for different terminations, highlighting the stiffening effect of O-based terminations. Reprinted with permission from ref. 99, copyright 2021, John Wiley & Sons.

environments that provides both active and corrosion-resistant sites. Here, "corrosion-resistant" referred specifically to retarded surface oxidation and reduced metal dissolution/leaching under electrochemical bias, consistent with diffusion-limited degradation pathways expected for chemically disordered (high-entropy) lattices.

Defects introduce a second, closely coupled level of control. Point defects on the M, X or termination sublattices, antisite defects and extended defects such as grain boundaries all alter local coordination and charge distribution, thereby modifying both catalytic activity and stability.[89,94–97] Atomistic simulations of OH-terminated MXenes under load illustrate how terminations and defects together govern mechanical response: in a model tribological heterostructure, the interlayer H–H and O–H distances remained nearly constant under increasing pressure, indicating that hydrogen bonding between opposing terminations plays a dominant role in controlling layer spacing and shear behaviour (Fig. 13D).[98] Such mechanically robust, hydrogen-bonded interfaces are particularly attractive for HE-MXene electrodes that must tolerate repeated gas evolution, volume changes and bubble detachment during HER or OER without delamination.

The available defect-termination design space is further expanded by recent synthesis developments. Moving from concentrated HF to mixed-acid, non-aqueous or molten-salt etching allows one to reduce vacancy densities, access non-Al A-site chemistries and introduce less conventional terminations such as –N, –S, –Se or –Te, all of which are promising for tailoring adsorption and corrosion resistance in HE-Mxenes (Fig. 13E).[99] The same perspective shows that surface terminations also control mechanical properties: calculated 2D stiffness values for M_2CT_x monolayers vary strongly with both metal choice and termination, with O-terminated MXenes generally stiffer than their F-, OH- or Cl-terminated counterparts across the 3d–5d series (Fig. 13F).[47,61–64,99] Strong M–O bonding increases M–X bond strength and suppresses detrimental M–M interactions, whereas more ionic M–F or M–(OH) bonding has a much weaker stiffening effect.[87–89] For HE-MXenes, these trends imply that appropriately chosen O-rich termination ensembles can simultaneously enhance electrocatalytic activity and mechanical robustness, while controlled introduction of vacancies can be used to create additional active sites at the cost of some stiffness. Overall, surface terminations and defects in HE-MXenes should be treated as coupled, designable variables rather than unavoidable by-products of etching. High-throughput thermodynamic maps (Fig. 13A–C), tribological simulations (Fig. 13D) and mechanical modelling (Fig. 13E and F) together suggest a practical strategy: first select metal combinations and terminations that fall within the thermodynamic and mechanical stability windows, then use etching, post-treatment and electrochemical conditioning to engineer a controlled population of vacancies and mixed terminations on those multi-metal lattices. Systematically linking such termination–defect motifs to HER, OER or CO_2RR performance in HE-MXenes remains a major opportunity for future work in electrocatalysis for sustainable energy conversion.

5. High-entropy MXenes for hydrogen-related electrocatalysis

5.1 Hydrogen evolution activity and high-entropy MXene-based heterostructures

A central advantage of HE-MXenes for HER is that configurational disorder produces not a single hydrogen adsorption energy but a distribution of ΔG_{H*} values associated with different local metal–termination ensembles. High-throughput DFT calculations on high-entropy $M_2C(T)_2$ compositions (M = Ti, V, Nb, Mo, Ta; T = O, OH, F) showed that multi-metal mixing broadens the ΔG_{H*} spectrum on OH-terminated surfaces and increases the fraction of sites with near-optimal binding relative to monometallic $Ti_2C(T)_2$.[18] HE-MXenes can therefore act as multi-site HER platforms in which activity is governed by a statistically significant subset of favourable local motifs rather than by the average adsorption energy of the surface (Fig. 14A and B).

The clearest experimental HER demonstration so far is the V–Co_2P@HE heterostructure reported by Ma and co-workers.[31] In this design, single-layer $(TiVCrNbMo)_5C_4T_x$ HE-MXene was electrodeposited on Ni foam, followed by growth of V–Co layered hydroxide precursors and phosphidation to form a Co_2P nanonetwork strongly coupled to the HE-MXene scaffold (Fig. 14C). The HE-MXene served as a conductive and hydrophilic support, while interfacial coupling and V doping tuned the electronic structure of Co_2P and facilitated charge redistribution. XPS/XAS and DFT results indicated optimised water adsorption, reduced H_2O dissociation barriers, and more favourable H adsorption at the heterointerface, consistent with accelerated Volmer–Heyrovsky kinetics.

In 1 M KOH, V–Co_2P@HE required only ~33 mV to reach 10 mA cm^{-2} and showed a Tafel slope of ~47 mV dec^{-1}, outperforming Co_2P, Co_2P@HE, V–Co_2P and even Pt/C under the same conditions (Fig. 14D and E).[31] It also displayed good durability at high current density and enabled efficient overall water splitting when used as part of a bifunctional electrode pair (Fig. 14F). These results suggest that, for HER, HE-MXenes are most compelling when used as electronically active, multicomponent scaffolds that provide both distributed adsorption sites and strong interfacial coupling to catalytically active phosphide-, sulfide- or hydroxide-type phases. At present, this HE-MXene-based heterostructure strategy is

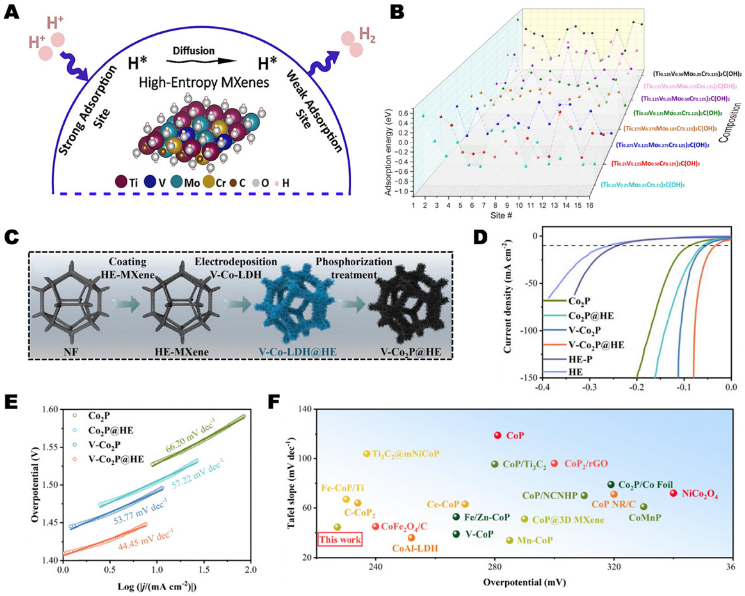

Fig. 14 HE-MXenes as multi-site HER platforms and conductive scaffolds. (A) Schematic of distributed H adsorption and diffusion on HE-MXene surfaces. (B) H adsorption energies on OH-terminated HE-MXenes, showing many near-optimal sites. Reprinted with permission from ref. 18, copyright 2025, Elsevier. (C) Synthesis of V–Co_2P@HE on Ni foam. (D) and (E) HER polarization and Tafel analysis of V–Co_2P@HE and reference catalysts. (F) HER comparison with representative non-noble catalysts. Reprinted with permission from ref. 31, copyright 2023, Elsevier.

better supported experimentally than claims of stand-alone HE-MXene HER catalysis.

5.2 Hydrogen oxidation reaction and reversible hydrogen electrodes

Direct studies of HE-MXenes for HOR have not yet been reported. Nevertheless, a concise design blueprint can be drawn from MXene-supported alkaline HOR catalysts, where conductive carbide surfaces and strong metal–support interactions help balance H* and OH* adsorption. A representative example is Ru–CuO/MXene supported on $Mo_2TiC_2T_x$ (Fig. 15A), which delivered higher alkaline HOR activity and better CO tolerance than commercial Pt/C (Fig. 15B and C) through interfacial charge redistribution at the Ru–O–Cu/MXene junction. 107 DFT and spectroscopic analyses showed that the heterointerface weakened H binding on Ru, strengthened OH binding on CuO, and lowered the overall HOR barrier (Fig. 15D–H).

For HE-MXenes, the relevance of this example is conceptual rather than demonstrative. Multi-metal M-sublattices and mixed terminations could provide additional handles to tune electronic metal–support interactions, stabilise Ru- or Pt-lean heterojunctions, and balance H/OH adsorption under alkaline HOR conditions. Future studies should therefore test whether HE-MXene supports can outperform conventional MXenes in reversible hydrogen electrodes by improving heterointerface stability, lowering noble-metal loading, and sustaining activity under oxidising anode conditions. Until such experiments are available, HOR should be regarded as a promising design direction for HE-MXenes rather than an experimentally established application.

6. High-entropy MXenes for oxygen electrocatalysis

OER and ORR remain key kinetic bottlenecks in water electrolysers, fuel cells and rechargeable metal–air batteries.[101] HE-MXenes are relevant to these reactions primarily as multicomponent conductive scaffolds and interfacial modulators, rather than as already established stand-alone oxygen electrocatalysts. Their multi-metal M-sublattices, mixed terminations and high conductivity can tune interfacial charge transfer, stabilise oxygen-active phases and broaden local adsorption environments, while direct experimental demonstrations of HE-MXenes in oxygen electrocatalysis are still limited.[18,30,102–104] Accordingly, this section centres on emerging HE-MXene-based oxygen-electrocatalytic architectures, with conventional MXene examples included only where they provide concise transferable design rules.[30,105,114,115]

6.1 Oxygen evolution reaction in water splitting and metal–air batteries

6.1.1 MXene–(oxy)hydroxide heterostructures as design guidance for HE-MXenes. MXene–(oxy)hydroxide hybrids illustrate how conductive 2D carbides can improve OER by promoting charge transport and interfacial coupling, even when the dominant redox centres remain in the hydroxide phase. In

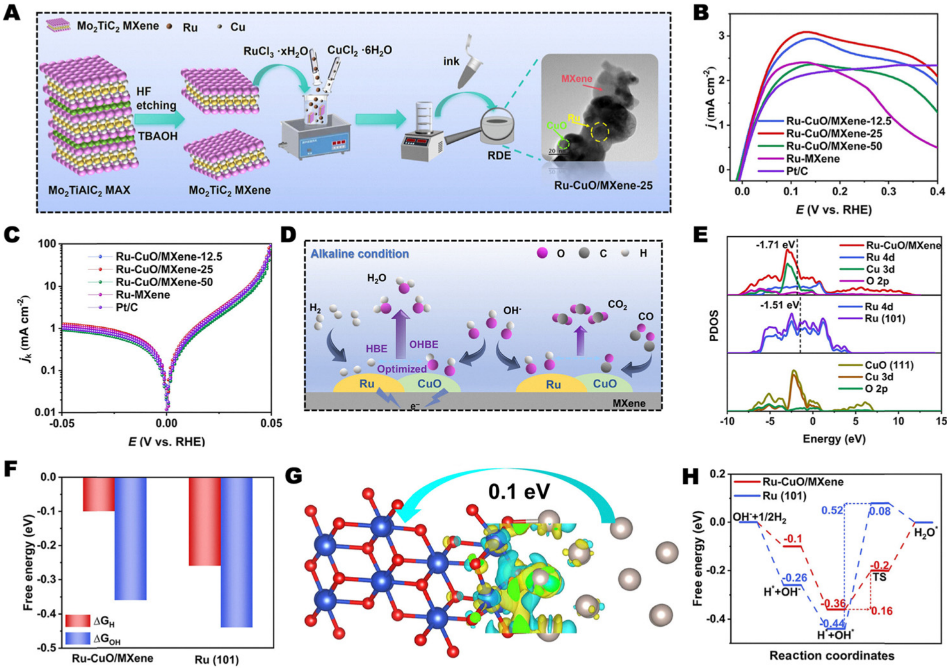

Fig. 15 Ru–CuO/MXene heterojunctions for alkaline HOR. (A) Synthesis and structure of Ru–CuO/MXene. (B) and (C) HOR polarization and Tafel analyses. (D) Proposed HOR mechanism with Ru and CuO sites for H* and OH* adsorption. (E)–(H) Electronic-structure, adsorption-energy, charge-density and free-energy analyses of Ru–CuO/MXene. Reprinted with permission from ref. 100, copyright 2024, American Chemical Society.

NiFe-LDH/Ti_3C_2 and LDH/MXNF-type systems, incorporation of Ti_3C_2 or Ti_3CN lowered OER overpotentials and Tafel slopes by improving LDH dispersion, reducing charge-transfer resistance and tuning the electronic environment of neighbouring Ni/Fe sites (Fig. 16B–E).[102,106] Likewise, H_2PO^{2-}/FeNi-LDH–V_2C nanohybrids showed that simultaneous modification of the hydroxide and MXene components can enhance OER activity and Zn–air battery cycling stability through strong interfacial Fe/Ni–O–V coupling (Fig. 16F–I).[103]

For the present, these systems are best regarded as design guidance rather than direct HE-MXene evidence. Their main message is that HE-MXenes need not be the sole oxygen-active phase; instead, they can function as electronically tunable, multicomponent supports for LDH- or oxyhydroxide-based catalysts, where high-entropy mixing on the MXene side may further diversify interfacial adsorption energetics and improve durability.

6.1.2 MXene–phosphide heterostructures and implications for HE-MXenes. MXene-supported phosphides provide a second instructive OER platform. NiFe-P/$Ti_3C_2T_x$ and CoFe–P/$Ti_3C_2T_x$ showed that strong phosphide/MXene coupling can reduce overpotential, improve kinetics and maintain structural integrity during alkaline OER, even though the active surface evolves toward oxyhydroxide-like species under operation (Fig. 17A–D).[107,108] These studies suggest a practical route for HE-MXene-based OER electrodes: multicomponent HE-MXene basal planes can be used as conductive scaffolds for multi-metal phosphides that reconstruct into compositionally rich oxyhydroxide shells during catalysis. At present, however, this remains a forward-looking design strategy rather than an experimentally established HE-MXene OER platform.

6.1.3 High-entropy oxide/MXene architectures as the most direct oxygen-related precedent. The most direct oxygen-electrocatalysis evidence comes from high-entropy oxide–MXene architectures. High-entropy borate oxides grown on $Ti_3C_2T_x$ showed improved OER performance relative to the oxide alone, indicating that the MXene scaffold enhances dispersion, charge transfer and structural stability under gas-evolving conditions (Fig. 18A–D).[19] Similarly, microwave-grown spinel HEO/$Ti_3C_2T_x$ hybrids displayed lower overpotentials and faster OER kinetics than their individual components, highlighting beneficial coupling between cation-disordered oxides and conductive MXene substrates (Fig. 18E and F).[30] These studies do not yet establish stand-alone HE-MXene OER catalysis, but they provide the clearest experimental support for the broader concept that high-entropy oxygen-active phases and MXene-based conductive scaffolds can be co-engineered for efficient oxygen electrocatalysis.

6.2 Oxygen evolution reaction in fuel cells and metal–air systems

Direct ORR studies using HE-MXenes themselves remain scarce, so current evidence is strongest for MXene-supported or MXene-derived architectures. A representative non-precious example is Co–S–N–C@MXene, where the $Ti_3C_2T_x$ substrate improves conductivity, active-site utilisation and durability, enabling ORR performance competitive with Pt/C in alkaline

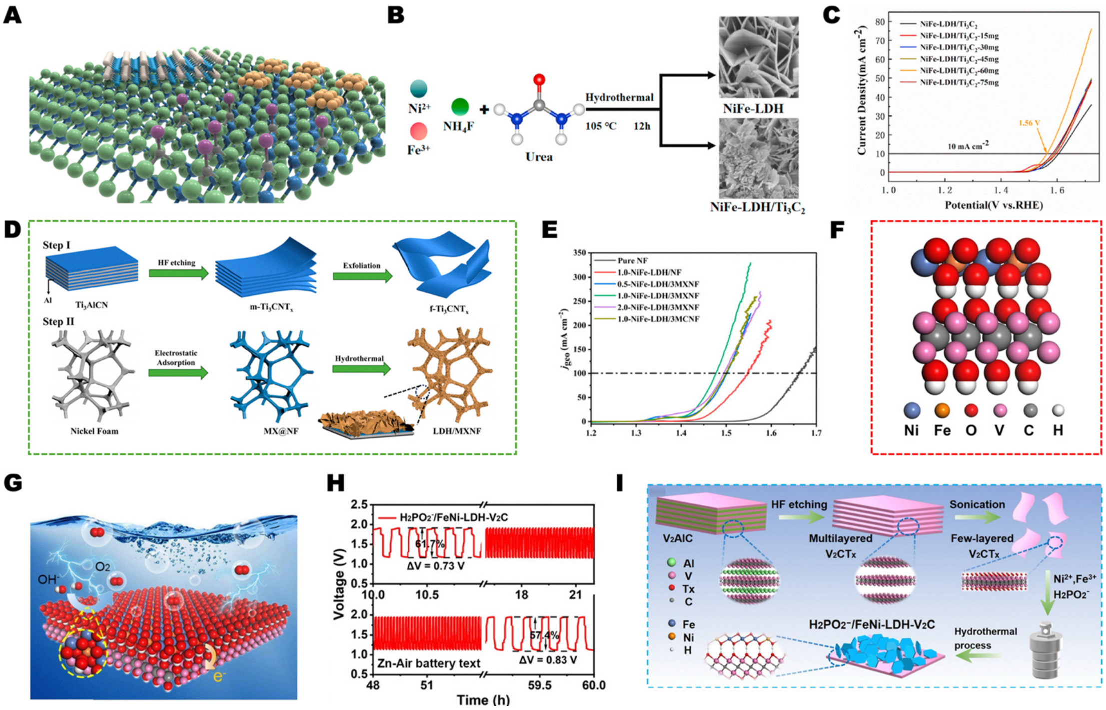

Fig. 16 Representative MXene-based OER architectures. (A) MXene platforms for OER, including 2D–2D stacks, single-atom sites and supported clusters. (B) and (C) NiFe-LDH/Ti_3C_2 synthesis and OER performance. Reprinted with permission from ref. 106, copyright 2024, Elsevier. (D) and (E) LDH/MXNF electrode fabrication and OER activity. Reprinted with permission from ref. 102, copyright 2024, MDPI. (F)–(I) $H_2PO_2^-$/FeNi-LDH–V_2C interface model, Zn–air battery concept, cycling stability and synthesis. Reprinted with permission from ref. 103, copyright 2021, Elsevier.

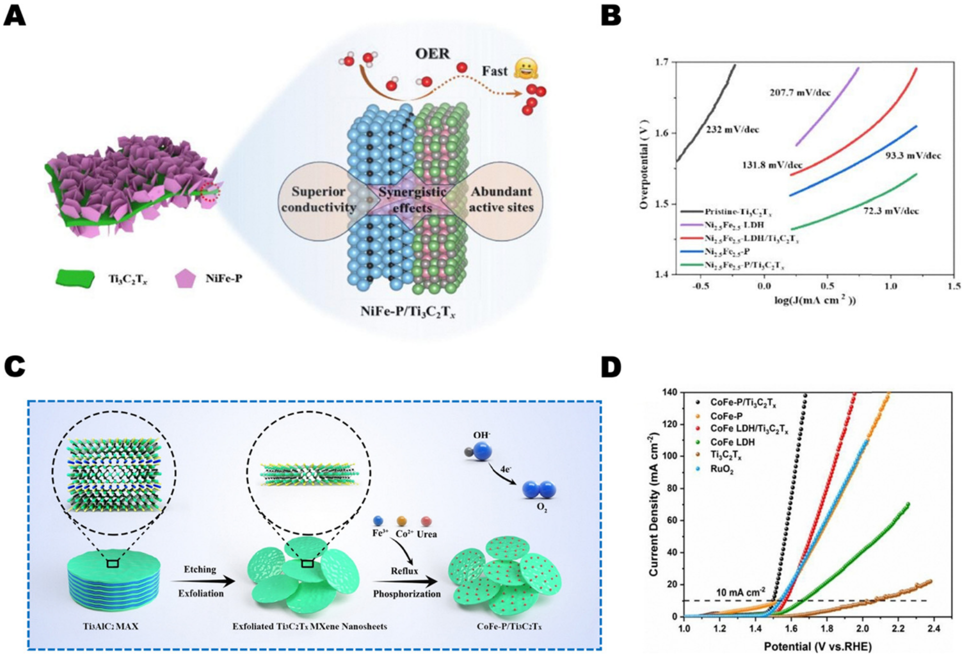

Fig. 17 MXene–phosphide heterostructures for alkaline OER. (A) Schematic of NiFe-P/$Ti_3C_2T_x$, where bimetallic phosphide nanostructures are anchored on conductive $Ti_3C_2T_x$ MXene. (B) Tafel plots showing faster OER kinetics for NiFe-P/$Ti_3C_2T_x$ than for reference catalysts. Reprinted with permission from ref. 107, copyright 2025, Elsevier. (C) Synthesis of CoFe–P/$Ti_3C_2T_x$ *via* CoFe-LDH growth on $Ti_3C_2T_x$ followed by phosphidation. (D) LSV curves showing improved OER performance of CoFe–P/$Ti_3C_2T_x$ relative to CoFe–P, CoFe-LDH, $Ti_3C_2T_x$ and RuO_2. Reprinted with permission from ref. 108, copyright 2022, John Wiley & Sons.

media and strong anion-exchange membrane fuel-cell output (Fig. 19A).[109] Although this is not an HE-MXene system, it shows how a conductive 2D carbide scaffold can stabilise dense populations of catalytic sites. A more relevant high-entropy example is the MXene-derived M–TiO_2/HEA heterojunction, in which laser treatment of metal-salt-loaded $Ti_3C_2T_x$ simultaneously generated TiO_2 and FeCoNiCrTi high-entropy alloy nanoparticles (Fig. 19B–D).[110] Strong coupling at the HEA/TiO_2/MXene interface improved oxygen-electrocatalytic behaviour and enabled durable photo-assisted Zn–air battery operation. This system is still not a direct demonstration of pristine HE-MXene ORR catalysis, but it illustrates how MXene-derived supports and high-entropy active phases can be integrated into bifunctional oxygen electrodes. The evidence in oxygen electrocatalysis presently supports a support- and interface-centred role for HE-MXenes and HE-MXene-inspired architectures. The most credible near-term direction is therefore not to claim established stand-alone HE-MXene OER/ORR catalysis, but to develop HE-MXenes as multicomponent conductive frameworks that stabilise high-entropy oxides, phosphides, alloys or related oxygen-active phases while tuning interfacial charge transfer, defect chemistry and structural durability.

7. High-entropy MXenes for other electrochemical conversion reactions

Beyond hydrogen and oxygen electrocatalysis, HE-MXenes are promising for selectivity-sensitive electrochemical transformations such as CO_2 reduction and nitrogen-related reactions, where the key challenge is to favour target intermediates while suppressing competing HER.[93,111,112] In principle, HE-MXenes are attractive because multi-metal mixing, mixed terminations and lattice distortion can generate a broad distribution of local adsorption environments and decouple the binding of *H from that of $^*CO_2$, *COOH, $^*N_2$ or *NNH.[18,22,35,37,38] However, direct experimental demonstrations of HE-MXenes in these reactions remain limited. Accordingly, this section focuses on the most relevant HE-MXene-specific insights and HE-MXene-based design opportunities, while conventional MXene and other high-entropy systems are discussed only briefly where they provide transferable mechanistic guidance.[93,111,113–117]

7.1 CO_2 reduction reaction

7.1.1 State-of-the-art MXene-based CO_2 reduction reaction catalysts and lessons for high-entropy design. Current MXene-based CO_2RR studies mainly establish design rules rather than direct HE-MXene evidence. O-terminated Ti-based MXenes can stabilise isolated or paired metal centres, suppress HER, and tune the relative energetics of $^*CO_2$, *COOH and *H through local coordination.[85,111,112,116] In particular, Ti_2CO_2-supported dual-atom catalysts showed that multi-metal cooperation can promote CO_2 activation and C–C coupling while maintaining weaker H adsorption (Fig. 20A and B).[118] Complementary descriptor-based studies on TM–Ti_2CO_2 and TM–Ov–Ti_2CO_2 single-atom catalysts further showed that subtle changes in the local TM–Ti–O environment strongly affect CO_2 activation and product selectivity (Fig. 20C and D).[119] These results are

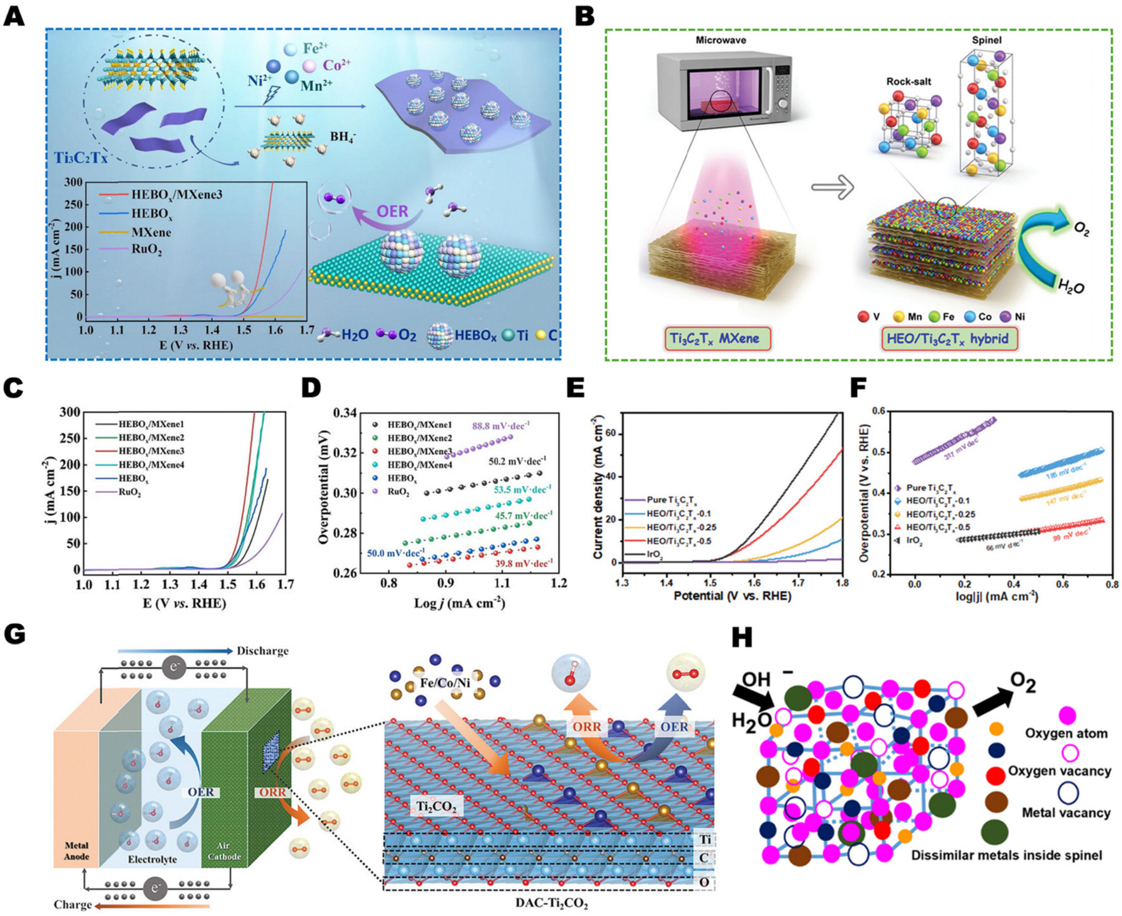

Fig. 18 Representative OER/ORR-related high-entropy oxide–MXene systems. (A) HEBO$_x$/Ti$_3$C$_2$T$_x$ for alkaline OER. Reprinted with permission from ref. 19, copyright 2024, Elsvier. (B) Microwave synthesis of spinel HEO/Ti$_3$C$_2$T$_x$ hybrids. Reprinted with permission from ref. 30, copyright 2023, John Wiley & Sons. (C) and (D) OER activity and kinetics of HEBO$_x$, HEBO$_x$/MXene and RuO$_2$. Reprinted with permission from ref. 19, copyright 2024, Elsvier. (E) and (F) LSV and Tafel analysis of Ti$_3$C$_2$T$_x$, HEO/Ti$_3$C2T$_x$ hybrids and IrO$_2$. Reprinted with permission from ref. 30, copyright 2023, John Wiley & Sons (G) MXene-supported double-atom catalysts in a rechargeable metal–air battery. Reprinted with permission from ref. 145, copyright 2021, John Wiley & Sons. (H) High-entropy spinel oxide with diverse local catalytic environments. Reprinted with permission from ref. 146, copyright 2024, American Chemical Society.

most useful as conceptual guidance: they indicate that HE-MXenes could extend the same principles by offering a broader set of local metal ensembles and electronically distinct adsorption motifs than single-metal MXenes.[86,133–135,145,146]

7.1.2 Conceptual advantages of high-entropy MXenes for CO$_2$ reduction reaction. The main opportunity for HE-MXenes in CO$_2$RR is not yet an established experimental one, but a design-space expansion. Potential–pH analysis of Ti$_3$C$_2$, Mo$_2$C and V$_2$C has shown that MXene surfaces are dynamically reconstructed under CO$_2$RR conditions, and that termination chemistry strongly influences competition between CO$_2$RR and HER (Fig. 21A and B).[120] Similarly, interfacial engineering strategies such as Ag intercalation into Ti$_3$C$_2$T$_x$ and single-atom metal anchoring on Ti$_2$CO$_2$ demonstrate that partially oxidised surfaces, metal–MXene coupling and well-defined local coordination can improve CO selectivity or lower the limiting potential for deeper CO$_2$ reduction (Fig. 21C–F).[121,122] In the context of HE-MXenes, these studies suggest three realistic advantages: (i) multi-metal M-sublattices can create a wider distribution of TM–O/C environments that may better balance *CO$_2$ and *H binding; (ii) mixed-metal carbides may better tolerate the partially oxidised or hydroxylated surfaces often encountered during CO$_2$RR; and (iii) HE-MXenes may serve as conductive, chemically active scaffolds for single atoms, dual atoms or small clusters. At present, these are best viewed as well-supported design directions rather than experimentally established HE-MXene CO$_2$RR performance.

7.2 Nitrogen reduction reaction and ammonia-related chemistry

7.2.1 MXene-based nitrogen reduction reaction: from Ti$_3$C$_2$-based catalysts to termination and single-atom engineering. As for CO$_2$RR, current MXene-based NRR studies primarily provide transferable lessons for HE-MXene design. Ti$_3$C$_2$T$_x$-based systems have shown that exposed edge sites, termination engineering and heterostructure formation can improve NH$_3$ selectivity by suppressing HER and facilitating cooperative N$_2$/H$_2$O activation. For example, vertically aligned Ti$_3$C$_2$T$_x$

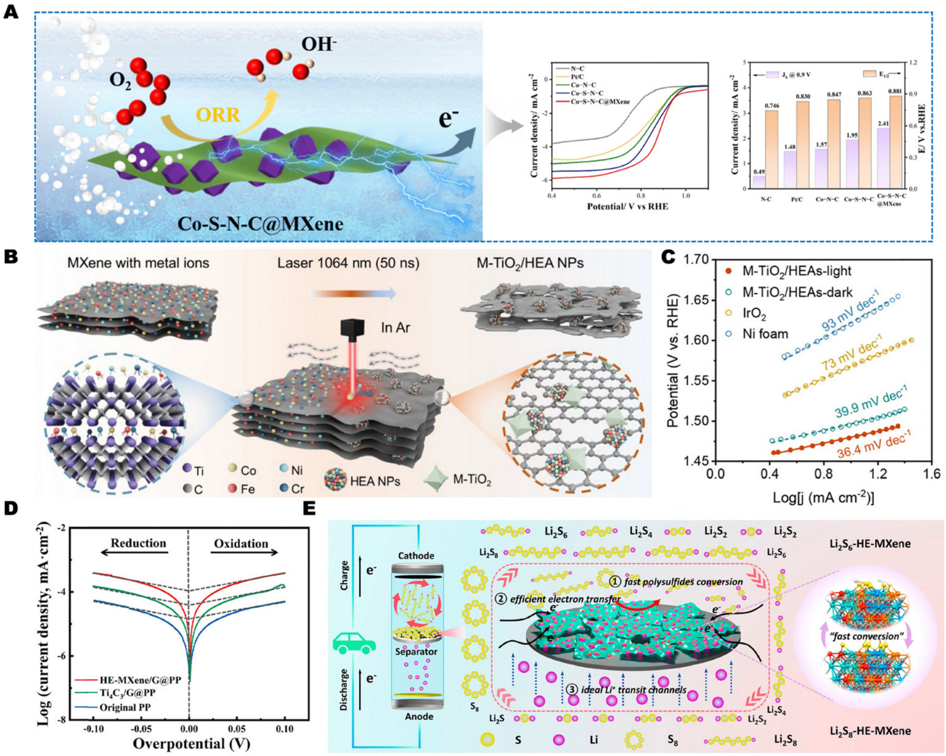

Fig. 19 MXene-based high-entropy architectures for advanced cathodic electrocatalysis. (A) ORR comparison of Co–S–N–C@MXene with reference catalysts in alkaline media. Reprinted with permission from ref. 109, copyright 2025, American Chemical Society. (B) Laser-pulse synthesis of TiO_2/high-entropy alloy heterostructures on $Ti_3C_2T_x$. (C) Tafel slope extracted from the OER polarization curves. (D) Corresponding Tafel plots of M-TiO_2/HEAs and reference catalysts, highlighting the improved oxygen electrocatalysis and light-assisted Zn–air battery performance. Reprinted with permission from ref. 110, copyright 2025, John Wiley & Sons. (E) Schematic illustration of HE-MXene/G@PP and its role in suppressing lithium polysulfide dissolution while promoting electron transfer in Li–S batteries. Reprinted with permission from ref. 15, copyright 2024, American Chemical Society.

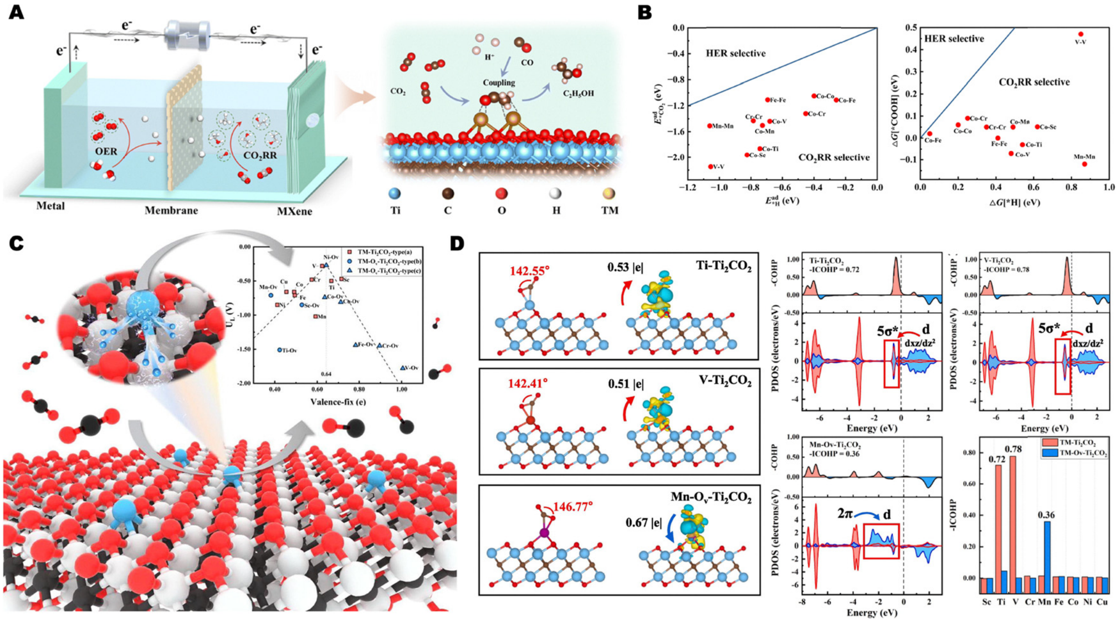

Fig. 20 MXene-based active-site concepts for HE-MXene CO_2RR. (A) CO_2RR cell and DACs on Ti_2CO_2 MXene. (B) Adsorption and reaction energetics identifying DACs/Ti_2CO_2 compositions selective for CO_2RR over HER. Reprinted with permission from ref. 118, copyright 2025, Royal Society of Chemistry. (C) TM–Ti–O descriptor for MXene-based SAC screening. (D) Electronic-structure analyses of Ti-, V- and Mn-modified Ti_2CO_2 surfaces. Reprinted with permission from ref. 119, copyright 2023, Elsevier.

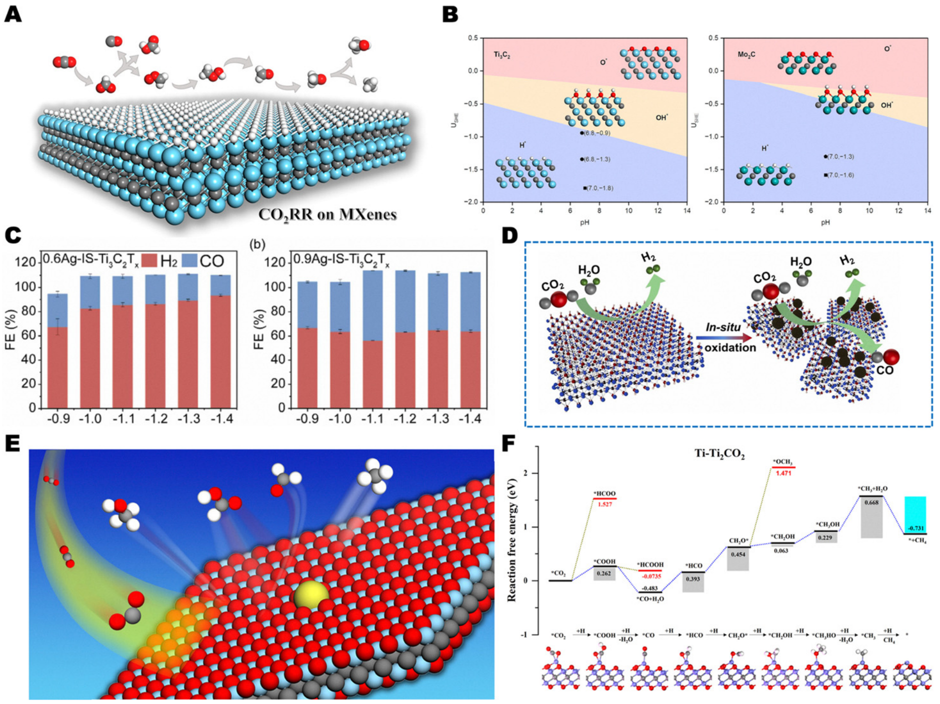

Fig. 21 Design concepts for MXene and HE-MXene CO$_2$RR catalysts. (A) CO$_2$RR/HER competition on terminated MXene surfaces. (B) Potential–pH phase diagrams of Ti$_3$C$_2$, Mo$_2$C and V$_2$C under CO$_2$RR conditions. Reprinted with permission from ref. 120, copyright 2024, American Chemical Society. (C) Faradaic efficiencies of H$_2$ and CO for Ag-intercalated Ti$_3$C$_2$T$_x$ and Ag/Ti$_3$C$_2$T$_x$ catalysts, showing selectivity tuning by interlayer engineering. (D) Illustration of *in situ* oxidation of nanostructured Ti$_3$C$_2$T$_x$ to form TiO$_x$/Ti$_3$C$_2$ heterostructures that modulate the electronic structure and enhance CO production. Reprinted with permission from ref. 121, copyright 2024, Elsevier. (E) MXene-based single-atom catalysts, where isolated transition-metal atoms anchored on O-terminated Ti$_2$CO$_2$ provide well-defined CO$_2$ activation sites. (F) Calculated free-energy profile for CO$_2$ reduction to CH$_4$ on Ti@Ti$_2$CO$_2$, highlighting the sequence of proton–electron transfer steps and the low limiting potential. Reprinted with permission from ref. 122, copyright 2023, American Chemical Society.

architectures and MXene/FeOOH hybrids identified favourable roles of edge Ti sites and neighbouring oxygenated motifs in NRR (Fig. 22C and D).[123] Surface tuning through TiFeO$_x$ overlayers further showed that removal of inactive F-rich terminations and creation of Fe–O–Ti interfacial motifs can markedly improve NH$_3$ yield and faradaic efficiency (Fig. 22E and F).[124] These studies do not constitute direct HE-MXene NRR evidence, but they show that termination control, edge-site exposure and cooperative interfacial motifs are likely to be central design elements when HE-MXenes are evaluated for ammonia electrosynthesis.

7.2.2 Lessons from high-entropy perovskites and sulfides in nitrogen chemistry.

High-entropy sulfides and oxides provide the clearest evidence that multi-metal disorder can improve nitrogen-related electrocatalysis, and these lessons are directly relevant to HE-MXenes. Increasing configurational entropy in high-entropy sulfides enhanced NH$_3$ production and improved electrochemical metrics such as charge-transfer resistance and double-layer capacitance (Fig. 22A and B).[125] More concrete examples come from nitrate- and nitrogen-reduction catalysts such as hollow NiCoFeV–S sulfides and vacancy-rich high-entropy perovskites, where multi-cation mixing and defect engineering improved NH$_3$ yield, faradaic efficiency and intermediate stabilisation (Fig. 23A–G).[126,127] These systems underline the value of distributed adsorption sites, vacancy-assisted activation and multi-metal electronic tuning. For HE-MXenes, the implication is again primarily strategic: future catalysts should combine the conductive, termination-tunable MXene backbone with controlled multi-metal mixing and defect chemistry to create selective environments for N-containing intermediates while limiting HER. Until direct demonstrations become more common, HE-MXenes in NRR and NO$_3$RR should therefore be regarded as a promising but still emerging direction.

10. Perspectives and concluding remarks

HE-MXenes have emerged as a distinct branch of MXene chemistry in which multi-metal lattices, rich defect structures and heterogeneous terminations are deliberately combined to modulate adsorption energies and reaction pathways for key electrochemical conversions. This review indicate that convincing proof-of-concept has already been obtained across HER/HOR, OER/ORR and small-molecule transformations such as CO$_2$RR and NRR, with activity and stability metrics that increasingly rival or complement conventional MXenes and selected noble-metal systems. At the same time, the field remains synthesis- and mechanism-limited: phase-pure HE-MAX precursors

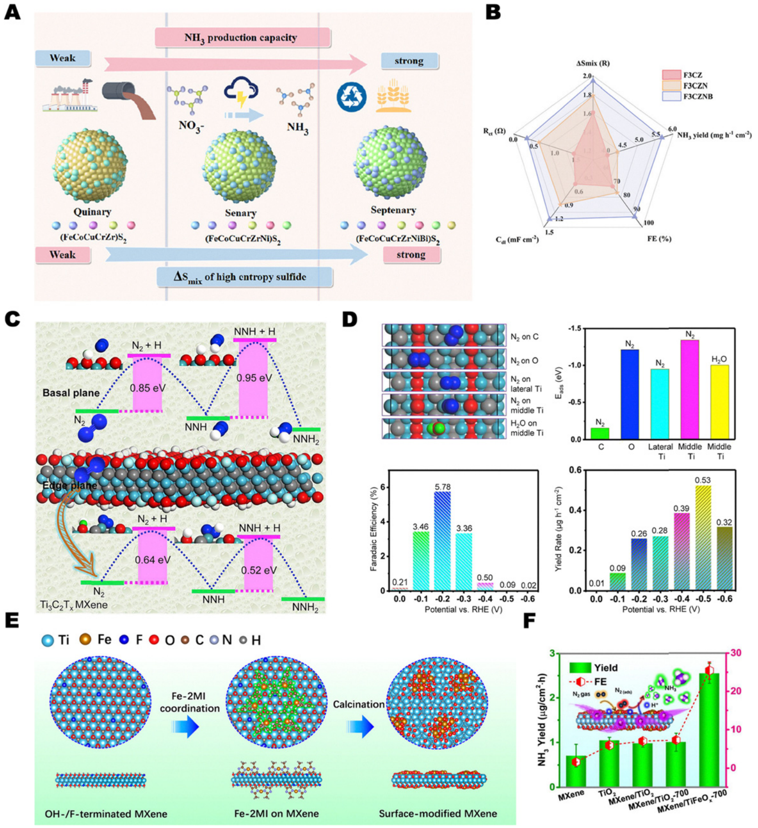

Fig. 22 (A) High-entropy and MXene-based NRR catalyst concepts. (A) Mixing-entropy-dependent NH_3 production in high-entropy sulfides. (B) Comparison of key NRR and electrochemical metrics for high-entropy sulfide catalysts. Reprinted with permission from ref. 125, copyright 2025, Elsevier. (C) $Ti_3C_2T_x$ nanosheets on a vertical metal host for ambient NRR. (D) Adsorption-site analysis and NRR performance of MXene/FeOOH hybrids. Reprinted with permission from ref. 123, copyright 2019, Elsevier. (E) Surface-tuned MXene/$TiFeO_x$ nanosheets. (F) NH_3 yield and FE of $TiFeO_x$-modified catalysts. Reprinted with permission from ref. 124, copyright 2020, American Chemical Society.

are difficult to prepare reproducibly, multi-step etching and delamination routes often compromise compositional integrity and termination control, and ensemble-averaged characterisation struggles to resolve the true distribution of local environments that govern catalytic behaviour. Most studies still rely on half-cell testing under modest current densities, leaving considerable uncertainty about long-term durability, degradation mechanisms and scalability in realistic devices.

Looking ahead, HE-MXenes can play a central role in sustainable electrocatalysis only if synthetic, mechanistic and device-level challenges are addressed in a coordinated way. More predictive approaches to composition selection and phase stability, greener and better-controlled etching strategies, and multi-scale *operando* characterisation will be essential to transform high-entropy design from an empirical concept into a rigorous framework for tailoring active sites and stabilising them under bias. Equally important is systematic benchmarking in electrolyzers, fuel cells, metal–air batteries and CO_2/NRR electrolysers under industrially relevant conditions, together with explicit consideration of element criticality, recyclability and life-cycle impacts. When combined with data-driven exploration of high-dimensional composition space and rational integration with other high-entropy and single-atom components, HE-MXenes have the potential to evolve from an emerging material class into a versatile platform for low-carbon energy technologies. In this context, several focused directions appear particularly important (Fig. 24):

(a) Phase stability calculations, high-throughput electronic-structure screening and ML-assisted evaluation of configurational-entropy descriptors (ΔS_{mix}, Ω, δ, ΔH_{mix}) should be coupled with combinatorial synthesis to identify composition windows that reliably yield single-phase HE-MAX precursors and robust HE-MXenes without extensive trial-and-error optimisation.

(b) Fluoride-free molten-salt, halogen, or electrochemical routes tailored to multi-metal carbides are needed to minimize preferential leaching and allow deliberate tuning of –O/–OH/–F/–Cl/–S terminations, while reducing the environmental burden and improving scalability relative to conventional HF or *in situ* HF protocols.

(c) Standard pipelines for HE-MXenes should integrate atomic-resolution STEM/EDS, pair-distribution-function analysis and *operando* XAS, XPS and vibrational spectroscopy under HER/HOR, OER/ORR, CO_2RR and NRR conditions, combined with microkinetic and Monte-Carlo models that explicitly treat distributions of adsorption energies rather than single descriptor values.

(d) Future studies should increasingly report performance in realistic membrane–electrode assemblies, metal–air cells

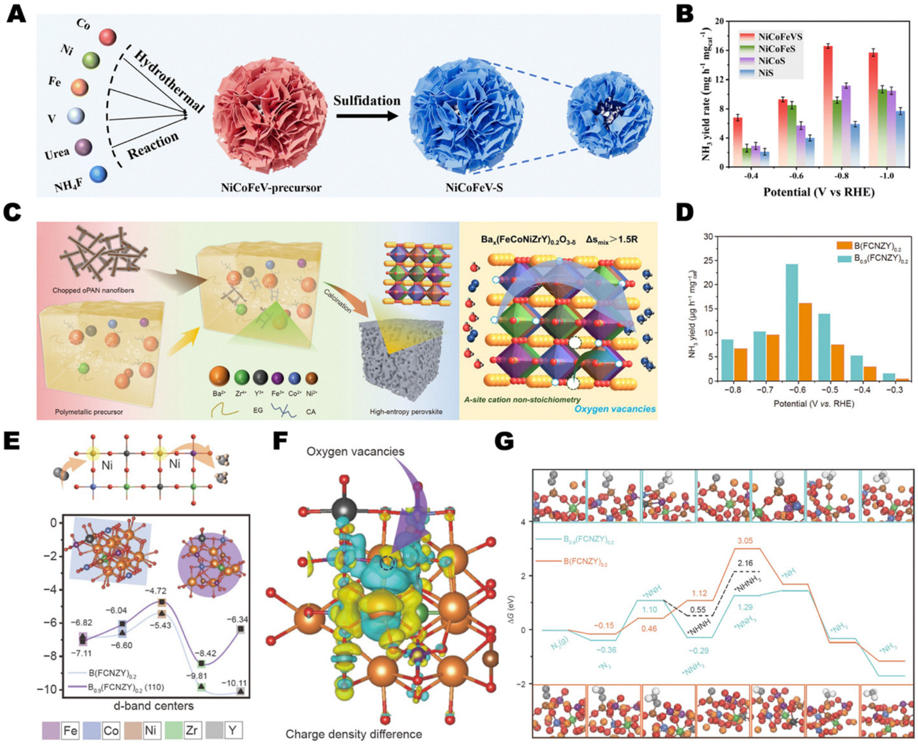

Fig. 23 High-entropy sulfide and perovskite catalysts for nitrate/nitrogen reduction. (A) Formation of hollow NiCoFeV–S high-entropy sulfide. (B) NH_3 yield showing improved activity of NiCoFeV–S over lower-entropy sulfides. Reprinted with permission from ref. 126, copyright 2025, Royal Society of Chemistry. (C) Synthesis of porous Bax$(FeCoNiZrY)_{0.2}O_{3-\delta}$ high-entropy perovskites. (D) NH_3 yield of stoichiometric and vacancy-rich perovskites. (E) d-Band-centre analysis of candidate active sites. (F) Charge–density difference near oxygen-vacancy-associated Ni sites. (G) Free-energy profiles for eNRR on stoichiometric and vacancy-rich surfaces. Reprinted with permission from ref. 127, copyright 2022, Springer Nature.

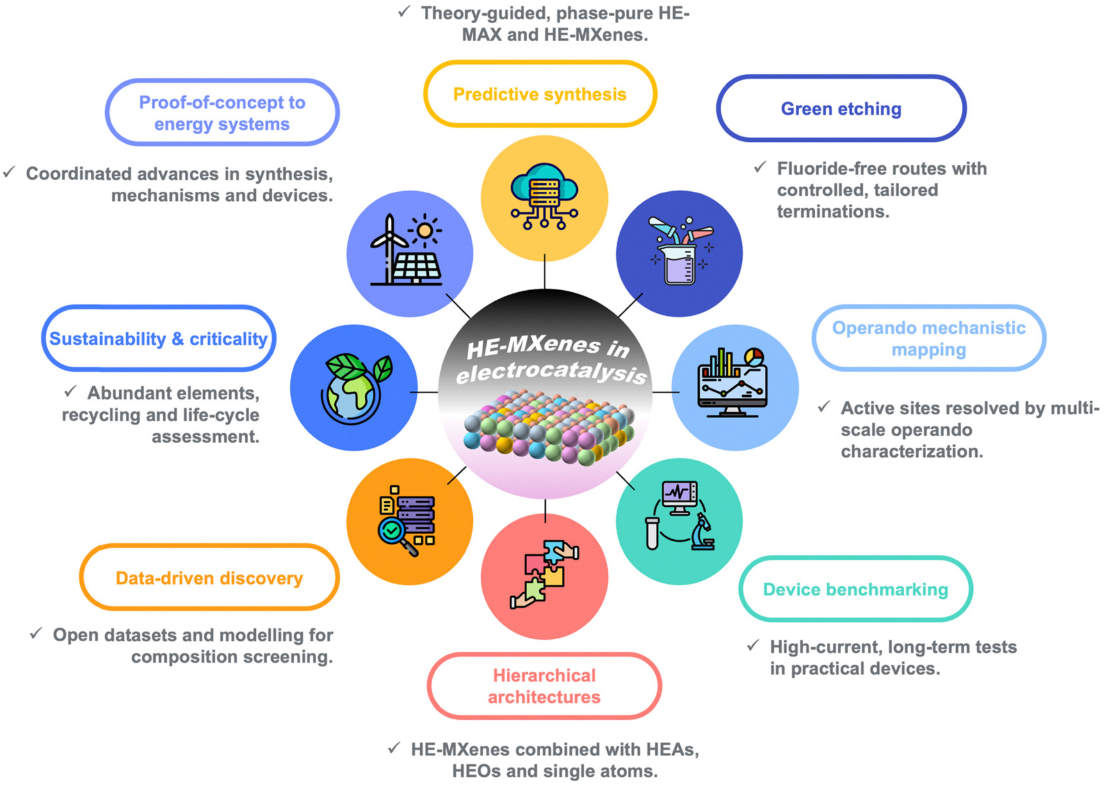

Fig. 24 Schematic depiction of the core effects, properties and future development directions of HE-MXenes in electrocatalysis.

and flow-cell reactors, including overpotentials at ≥500–1000 mA cm^{-2}, accelerated stress tests, gas-evolution and mass-transport effects, as well as post-mortem analysis of oxidation, metal dissolution, delamination and termination loss.

(e) Combining HE-MXenes with other high-entropy subsystems such as HEA nanoparticles, HEO or sulfides, and MXene-anchored single-atom centres offers a route to catalysts where activity, selectivity and stability emerge from cooperative interactions across multiple length scales, including possible self-healing or benign-oxidation behaviour under operation.

(f) Curated databases that capture full compositional statistics, synthesis conditions, structural and termination characterisation, and electrochemical protocols for HE-MXenes will enable interpretable ML models for property prediction and inverse design, provided that reporting standards are harmonised across laboratories.

(g) Many current HE-MXene formulations rely on elements such as Nb, Mo, Ta or noble metals. Future work should evaluate alternative, more abundant chemistries, develop recycling and regeneration strategies for spent electrodes, and integrate techno-economic and life-cycle assessments into materials selection and device design.

Alignment of these efforts is expected to convert HE-MXenes from an emerging scientific curiosity into a mature, versatile platform for electrocatalytic hydrogen, oxygen and small-molecule conversion within sustainable energy systems.

Author contributions

Muhammad Yousuf: writing – original draft, resources. Xiaopeng Liu: review and editing. Connor W. Schroeder: review and editing. Jonathan Tjioe: review and editing. Yurui Liu: review and editing. Yue Wu: writing – review & editing, project administration, supervision.

Conflicts of interest

There are no conflicts to declare.

Data availability

No primary research findings, software, or code were included, and no new data were generated or analysed in this review.

Acknowledgements

Prof. Yue Wu thanks the support of the Herbert L. Stiles Professorship from Iowa State University and NSF CBET 241425.

Notes and references

1 L. Gao, Y. Wei, J. Zhang, Y. Ou and L. Chen, *Coord. Chem. Rev.*, 2026, **553**, 217569.

2 L. Dadsena, T. Maharana and S. E. Jujjavarapu, *Environ. Res.*, 2026, 123764.

3 W. Wang, X. X. Zhang, T. Yu, R. Guo and X. Liu, *J. Energy Storage*, 2026, **145**, 119807.

4 X. Liang, T. Zhou, L. Liu, H. Shui, S. Zhang, Y. Zheng and L. Li, *Int. J. Hydrogen Energy*, 2026, **207**, 153449.

5 R. Yang, J. Liu, M. Lin and P. Zeng, *Global Energy Interconnection*, 2026, **9**, 159–185.

6 Z.-Y. Tian, M. Yousuf, Z.-M. Wang, R. Jabeen, A. E. Mansy, S. Daniel and R. Kumar, in *Environmental Chemistry: Advanced Concepts and Applications*, ed. Z.-Y. Tian, Springer Nature, Singapore, 2025, pp. 15–41.

7 Y. Zhao, J. Zhang, X. Guo, X. Cao, S. Wang, H. Liu and G. Wang, *Chem. Soc. Rev.*, 2023, **52**, 3215–3264.

8 M. Yousuf, Z. Y. Tian, Z. M. Wang, R. Jabeen, A. E. Mansy, S. Daniel and R. Kumar, in *Environmental Chemistry: Advanced Concepts and Applications*, ed. Z. Y. Tian, Springer Nature, Singapore, 2025, pp. 43–66.

9 Z. Y. Tian, M. Yousuf, Z. M. Wang, R. Jabeen, A. E. Mansy, S. Daniel and R. Kumar, in *Environmental Chemistry: Advanced Concepts and Applications*, ed. Z. Y. Tian, Springer Nature, Singapore, 2025, pp. 1–14.

10 D. Li, C. Liu, S. Tao, J. Cai, B. Zhong, J. Li, W. Deng, H. Hou, G. Zou and X. Ji, *Nanomicro Lett.*, 2024, **17**, 22.

11 X. Yan, Y. Zhou and S. Wang, *Adv. Funct. Mater.*, 2025, **35**, 2413115.

12 J. T. Ren, L. Chen, H. Y. Wang and Z. Y. Yuan, *Chem. Soc. Rev.*, 2023, **52**, 8319–8373.

13 M. Naguib, M. Kurtoglu, V. Presser, J. Lu, J. Niu, M. Heon, L. Hultman, Y. Gogotsi and M. W. Barsoum, *Adv. Mater.*, 2011, **23**, 4248–4253.

14 W. Ma, Z. Qiu, M. Wang, C. Tan, L. Hu, X. Lv, Q. Li, J. Li and J. Dang, *Scr. Mater.*, 2023, **235**, 115596.

15 Q. Liang, S. Wang, X. Lu, X. Jia, J. Yang, F. Liang, Q. Xie, C. Yang, J. Qian, H. Song and R. Chen, *ACS Nano*, 2024, **18**, 2395–2408.

16 W. Song, D. Wang, S. Xiao, X. He, W. Xiong and J. Shen, *Mater. Des.*, 2024, **240**, 112857.

17 Z. Li, Y. Xiao, P. R. Chowdhury, Z. Wu, T. Ma, J. Z. Chen, G. Wan, T. H. Kim, D. Jing, P. He, P. J. Potdar, L. Zhou, Z. Zeng, X. Ruan, J. T. Miller, J. P. Greeley, Y. Wu and A. Varma, *Nat. Catal.*, 2021, **4**, 882–891.

18 M. H. Ghoncheh, Z. W. Chen, P. G. Demingos and C. V. Singh, *iScience*, 2025, **28**, 113436.

19 X. Li, H. He, Y. Yu, Z. Wang, R. Zheng, H. Sun, Y. Liu and D. Wang, *Appl. Surf. Sci.*, 2024, **645**, 158838.

20 D. Singh, S. Razzaq, E. Tayyebi and K. S. Exner, *ACS Catal.*, 2025, **15**, 5589–5600.

21 B. Anasori and Y. Gogotsi, *Graphene 2D Mater.*, 2022, **7**, 75–79.

22 S. K. Nemani, B. Zhang, B. C. Wyatt, Z. D. Hood, S. Manna, R. Khaledialidusti, W. Hong, M. G. Sternberg, S. K. R. S. Sankaranarayanan and B. Anasori, *ACS Nano*, 2021, **15**, 12815–12825.

23 J. W. Yeh, S. K. Chen, S. J. Lin, J. Y. Gan, T. S. Chin, T. T. Shun, C. H. Tsau and S. Y. Chang, *Adv. Eng. Mater.*, 2004, **6**, 299–303.

24 C. M. Rost, E. Sachet, T. Borman, A. Moballegh, E. C. Dickey, D. Hou, J. L. Jones, S. Curtarolo and J.-P. Maria, *Nat. Commun.*, 2015, **6**, 8485.

25 L. Zhang, J. Shi, K. Niu, P. Jia, Y. Gao and G. Gao, *ACS Appl. Nano Mater.*, 2023, **6**, 20812–20822.

26 K. Li, P. Hao, Q. Zhang, Y. Wang, J. Zhang, S. Dmytro and Y. Zhou, *Mater. Today Commun.*, 2024, **38**, 108255.

27 L. Zhang, H. Li, X. Zhang, C. Liu, Y. Sun, Y. Zhang, Z. Fang, J. He, R. Wang, K. Jiang and D. Chen, *Angew. Chem., Int. Ed.*, 2025, **64**, e202418538.

28 W. Xu, H. Chen, K. Jie, Z. Yang, T. Li and S. Dai, *Angew. Chem., Int. Ed.*, 2019, **58**, 5018–5022.

29 Z. Du, C. Wu, Y. Chen, Z. Cao, R. Hu, Y. Zhang, J. Gu, Y. Cui, H. Chen, Y. Shi, J. Shang, B. Li and S. Yang, *Adv. Mater.*, 2021, **33**, 2101473.

30 C. E. Park, R. A. Senthil, G. H. Jeong and M. Y. Choi, *Small*, 2023, **19**, 2207820.

31 W. Ma, Z. Qiu, J. Li, L. Hu, Q. Li, X. Lv and J. Dang, *J. Energy Chem.*, 2023, **85**, 301–309.

32 T. A. A. Batchelor, T. Löffler, B. Xiao, O. A. Krysiak, V. Strotkötter, J. K. Pedersen, C. M. Clausen, A. Savan, Y. Li, W. Schuhmann, J. Rossmeisl and A. Ludwig, *Angew. Chem., Int. Ed.*, 2021, **60**, 6932–6937.

33 L. Li, Z. Gao, W. Kang, Y. Feng, M. Hou, P. Yin, H. Liu and Z. Zhang, *Sci. China Mater.*, 2025, 1–9.

34 Y. Cui, Y. Zhang, Z. Cao, J. Gu, Z. Du, B. Li and S. Yang, *SusMat*, 2022, **2**, 65–75.

35 S. K. Nemani, M. Torkamanzadeh, B. C. Wyatt, V. Presser and B. Anasori, *Commun. Mater.*, 2023, **4**, 16.

36 Y. Sun and S. Dai, *Sci. Adv.*, 2021, **7**, eabg1600.

37 X. Zhao, Y. Chen, M. Feng, C. Xu, J. Du, X. Wang and Z. Liu, *J. Alloys Compd.*, 2024, **992**, 174586.

38 F. Yu, Y. Wang, K. Zhang, H. Shen, Y. Zhang, Z. Yang, G. Zeng, D. Cui, J. Xia, J. Liu, J. Li, M. Yang, H. Liu, C. Guo, W. Bao, K. Sun and J. Li, *J. Mater. Chem. A*, 2025, **13**, 28699–28717.

39 J. Zhou, Q. Tao, B. Ahmed, J. Palisaitis, I. Persson, J. Halim, M. W. Barsoum, P. O. Å. Persson and J. Rosen, *Chem. Mater.*, 2022, **34**, 2098–2106.

40 A. S. Etman, J. Zhou and J. Rosen, *Electrochem. Commun.*, 2022, **137**, 107264.

41 L. Gao, C. Li, W. Huang, S. Mei, H. Lin, Q. Ou, Y. Zhang, J. Guo, F. Zhang, S. Xu and H. Zhang, *Chem. Mater.*, 2020, **32**, 1703–1747.

42 C. Tsounis, P. V. Kumar, H. Masood, R. P. Kulkarni, G. S. Gautam, C. R. Müller, R. Amal and D. A. Kuznetsov, *Angew. Chem., Int. Ed.*, 2023, **62**, e202210828.

43 L. Qiao, J. Bi, G. Liang, Y. Yang, H. Wang and S. Wang, *J. Adv. Ceram.*, 2023, **12**, 1902–1918.

44 Z. Leong, H. Jin, Z. M. Wong, K. Nemani, B. Anasori and T. L. Tan, *Chem. Mater.*, 2022, **34**, 9062–9071.

45 M. Xu, Q. Zhu, Y. Li, Y. Gao, N. Sun and B. Xu, *Energy Environ. Sci.*, 2024, **17**, 7735–7748.

46 W. Huang, K. Shen, C. Liu, C. Xu and J. Cheng, *ACS Appl. Nano Mater.*, 2025, **9**, 704–711.

47 L. Chen, Y. Li, K. Liang, K. Chen, M. Li, S. Du, Z. Chai, M. Naguib and Q. Huang, *Small Methods*, 2023, **7**, 2300054.

48 J. Zhou, M. Dahlqvist, J. Björk and J. Rosen, *Chem. Rev.*, 2023, **123**, 13291–13322.

49 M. Yousuf, M. F. Arshad and Z. Tian, *Int. J. Chem. Kinet.*, 2024, **56**, 310–322.

50 A. Zhou, Y. Liu, S. Li, X. Wang, G. Ying, Q. Xia and P. Zhang, *J. Adv. Ceram.*, 2021, **10**, 1194–1242.

51 A. H. Lashkari, A. Ostovari Moghaddam, M. Naseri and A. Shokuhfar, *J. Mater. Res. Technol.*, 2023, **24**, 5024–5031.

52 Q. Tao, J. Lu, M. Dahlqvist, A. Mockute, S. Calder, A. Petruhins, R. Meshkian, O. Rivin, D. Potashnikov, E. N. Caspi, H. Shaked, A. Hoser, C. Opagiste, R. M. Galera, R. Salikhov, U. Wiedwald, C. Ritter, A. R. Wildes, B. Johansson, L. Hultman, M. Farle, M. W. Barsoum and J. Rosen, *Chem. Mater.*, 2019, **31**, 2476–2485.

53 L. Wang, H. Zhang, B. Wang, C. Shen, C. Zhang, Q. Hu, A. Zhou and B. Liu, *Electron. Mater. Lett.*, 2016, **12**, 702–710.

54 J. Halim, M. R. Lukatskaya, K. M. Cook, J. Lu, C. R. Smith, L. Å. Näslund, S. J. May, L. Hultman, Y. Gogotsi, P. Eklund and M. W. Barsoum, *Chem. Mater.*, 2014, **26**, 2374–2381.

55 J. Yang, M. Naguib, M. Ghidiu, L. M. Pan, J. Gu, J. Nanda, J. Halim, Y. Gogotsi and M. W. Barsoum, *J. Am. Ceram. Soc.*, 2016, **99**, 660–666.

56 M. Alhabeb, K. Maleski, T. S. Mathis, A. Sarycheva, C. B. Hatter, S. Uzun, A. Levitt and Y. Gogotsi, *Angew. Chem., Int. Ed.*, 2018, **57**, 5444–5448.

57 F. Liu, J. Zhou, S. Wang, B. Wang, C. Shen, L. Wang, Q. Hu, Q. Huang and A. Zhou, *J. Electrochem. Soc.*, 2017, **164**, A709.

58 S. Kajiyama, L. Szabova, H. Iinuma, A. Sugahara, K. Gotoh, K. Sodeyama, Y. Tateyama, M. Okubo and A. Yamada, *Adv. Energy Mater.*, 2017, **7**, 1601873.

59 F. Du, H. Tang, L. Pan, T. Zhang, H. Lu, J. Xiong, J. Yang and C. (John) Zhang, *Electrochim. Acta*, 2017, **235**, 690–699.

60 A. Vahidmohammadi, A. Hadjikhani, S. Shahbazmohamadi and M. Beidaghi, *ACS Nano*, 2017, **11**, 11135–11144.

61 J. Zhou, X. Zha, X. Zhou, F. Chen, G. Gao, S. Wang, C. Shen, T. Chen, C. Zhi, P. Eklund, S. Du, J. Xue, W. Shi, Z. Chai and Q. Huang, *ACS Nano*, 2017, **11**, 3841–3850.

62 N. Chen, Z. Duan, W. Cai, Y. Wang, B. Pu, H. Huang, Y. Xie, Q. Tang, H. Zhang and W. Yang, *Nano Energy*, 2023, **107**, 108147.

63 L. Liu, M. Orbay, S. Luo, S. Duluard, H. Shao, J. Harmel, P. Rozier, P. L. Taberna and P. Simon, *ACS Nano*, 2021, **16**, 111–118.

64 A. Gentile, S. Marchionna, M. Balordi, G. Pagot, C. Ferrara, V. Di Noto and R. Ruffo, *ChemElectroChem*, 2022, **9**, e202200891.

65 K. Arole, J. W. Blivin, A. M. Bruce, S. Athavale, I. J. Echols, H. Cao, Z. Tan, M. Radovic, J. L. Lutkenhaus and M. J. Green, *Chem. Commun.*, 2022, **58**, 10202–10205.

66 Y. Wang, L. Li, M. Shen, R. Tang, J. Zhou, L. Han, X. Zhang, L. Zhang, G. Kim and J. Q. Wang, *Adv. Sci.*, 2023, **10**, 2303693.

67 H. Xu, H. Shou, Z. Yan, K. Zhu, C. Wu, W. Jiang, Z. Liu, S. Wei, J. Shi, H. Akhtar, C. Wang and L. Song, *Adv. Mater.*, 2025, **37**, 2504586.

68 H. Kim, D. Gwon, D. Kim, J. Kee and J. Koo, *Adv. Mater. Technol.*, 2024, **9**, 2301437.

69 K. Montazeri, H. Badr, K. Ngo, K. Sudhakar, T. Elmelegy, J. Uzarski, V. Natu and M. W. Barsoum, *J. Phys. Chem. C*, 2023, **127**, 10391–10397.

70 A. Thakur, N. Chandran B.S., K. Davidson, A. Bedford, H. Fang, Y. Im, V. Kanduri, B. C. Wyatt, S. K. Nemani, V. Poliukhova, R. Kumar, Z. Fakhraai and B. Anasori, *Small Methods*, 2023, **7**, 2300030.

71 Y. N. Athreya, Effect of CTAB intercalation on electrochemical properties of $Ti_3C_2T_x$ MXene, MS thesis, Drexel University, 2025, DOI: 10.17918/00010916.

72 S. Nouseen and M. Pumera, *J. Mater. Chem. A*, 2025, **13**, 34055–34084.

73 Q. Fan, M. Chen, L. Li, M. Li, C. Xiao, T. Zhao, L. Pan, N. Liang, Q. Huang, L. Yu, L. Zhu, M. Naguib and K. Liang, *Nat. Commun.*, 2025, **16**, 5051.

74 A. Inman, K. Shevchuk, M. Anayee, W. Hammill, J. Lee, M. Saraf, C. E. Shuck, C. M. Armstrong, Y. He, T. Jin, M. Shekhirev, J. Capobianco and Y. Gogotsi, *Chem. Eng. J.*, 2023, **475**, 146089.

75 Z. Zhou, L. Wei, Y. Yi, S. Feng, Z. Zhan, D. Tian and C. Lu, *J. Materiomics*, 2023, **9**, 1151–1159.

76 A. Inman, V. Šedajová, K. Matthews, J. Gravlin, J. Busa, C. E. Shuck, A. VahidMohammadi, A. Bakandritsos, M. Shekhirev, M. Otyepka and Y. Gogotsi, *J. Mater. Res.*, 2022, **37**, 4006–4016.

77 X. Sang, Y. Xie, M. W. Lin, M. Alhabeb, K. L. Van Aken, Y. Gogotsi, P. R. C. Kent, K. Xiao and R. R. Unocic, *ACS Nano*, 2016, **10**, 9193–9200.

78 D. Yang, Y. Wang, X. Liu, Y. Gao, Y. Chen, G. Tian, S. Wang, L. Zhang and N. Tang, *Electrochim. Acta*, 2025, **536**, 146759.

79 A. Kuzmin, in *High-Entropy Alloys: Design, Manufacturing, and Emerging Applications*, ed. G. Yasin, M. Abubaker Khan, M. Ahmed Afifi, T. A. Nguyen and Y. Zhang, Elsevier, 2024, pp. 121–155.

80 K. Li, P. Hao, K. Yuan, T. Yao, J. Zhang and Y. Zhou, *Comput. Mater. Sci.*, 2023, **227**, 112271.

81 Samia, M. H. Jameel, M. Arain, I. Hussain, M. B. Hanif, S. Atri, M. Z. H. Mayzan and H. Dai, *Nano Mater. Sci.*, 2025, **7**, 444–481.

82 M. Liu, L. Yang, Z. Wu, G. Chen, X. Wang, X. Yang, G. Liang and R. Che, *Nat. Commun.*, 2025, **16**, 5633.

83 R. B. Araujo and T. Edvinsson, *J. Mater. Chem. A*, 2023, **11**, 12973–12983.

84 H.-B. Cui, Y. Wang, Y.-C. Wang, C. Chen, G. Guan and M.-Y. Han, *ACS Nano*, 2025, **19**, 40641–40661.

85 B. Guo, Z. Zhou, W. Sun and X. Hu, *iScience*, 2025, **28**, 113577.

86 P. Sharma, P. Singh and G. Balasubramanian, *Carbon*, 2024, **223**, 119015.

87 H. Mei, Y. Zhang, P. Zhang, A. G. Ricciardulli, P. Samorì and S. Yang, *Adv. Sci.*, 2024, **11**, 2409404.

88 F. Gu, W. Wang, H. Meng, Y. Liu, L. Zhuang, H. Yu and Y. Chu, *Matter*, 2025, **8**, 102004.

89 M. Tang, J. Li, Y. Wang, W. Han, S. Xu, M. Lu, W. Zhang and H. Li, *Symmetry*, 2022, **14**, 2232.

90 E. Rems, Y. J. Hu, Y. Gogotsi and R. Dominko, *Chem. Mater.*, 2024, **36**, 10295–10306.

91 E. M. Ahmed, A. S. Ali, E. M. Hieba, Z. S. Shaban, M. S. Fathy, A. M. Amer, A. M. Ishmael, A. Bakr, H. R. M. Rashdan and A. Elzwawy, *RSC Adv.*, 2025, **15**, 44812–44863.

92 H. Li, Y. Chen and Q. Tang, *ChemPhysChem*, 2024, **25**, e202400255.

93 L. Meng, E. Tayyebi, K. S. Exner, F. Viñes and F. Illas, *ChemElectroChem*, 2024, **11**, e202300598.

94 Q. Wang, S. Qiao, C. Huang, X. Wang, C. Cai, G. He and F. Zhang, *ACS Appl. Mater. Interfaces*, 2024, **16**, 24502–24513.

95 N. Li, S. Wei, Y. Xu, J. Liu, J. Wu, G. Jia and X. Cui, *Electrochim. Acta*, 2018, **290**, 364–368.

96 B. Zhang, J. Shan, X. Wang, Y. Hu and Y. Li, *Small*, 2022, **18**, 2200173.

97 M. Jussambayev, K. Shakenov, S. Sultakhan, U. Zhantikeyev, K. Askaruly, K. Toshtay and S. Azat, *Carbon Trends*, 2025, **19**, 100471.
98 Q. Yang, S. J. Eder, A. Martini and P. G. Grützmacher, *npj Mater. Degrad.*, 2023, **7**, 6.
99 B. C. Wyatt, A. Rosenkranz and B. Anasori, *Adv. Mater.*, 2021, **33**, 2007973.
100 J. Liu, Y. Xiang, S. Fang, Z. Du, Z. Li, L. Gao, F. Fu, L. Lv, X. Gao, J. Zhou, D. Wu and X. Jian, *ACS Appl. Mater. Interfaces*, 2024, **16**, 70508–70519.
101 Y. Zhao, D. P. Adiyeri Saseendran, C. Huang, C. A. Triana, W. R. Marks, H. Chen, H. Zhao and G. R. Patzke, *Chem. Rev.*, 2023, **123**, 6257–6358.
102 L. He, Q. Tang, Q. Fan, H. Zhuang, S. Wang, Y. Pang and K. Liang, *Catalysts*, 2024, **14**, 708.
103 Y. Chen, H. Yao, F. Kong, H. Tian, G. Meng, S. Wang, X. Mao, X. Cui, X. Hou and J. Shi, *Appl. Catal., B*, 2021, **297**, 120474.
104 A. Liu, X. Liang, X. Ren, W. Guan and T. Ma, *Electrochem. Energy Rev.*, 2021, **5**, 112–144.
105 P. V. Hlophe, H. Zhao, G. Li, K. N. Nigussa, S. Song and P. F. Msomi, *Carbon Trends*, 2025, **21**, 100594.
106 Y. Sun, Z. Wang, Q. Zhou, X. Li, D. Zhao, B. Ding and S. Wang, *Heliyon*, 2024, **10**, e30966.
107 L. Tan, J. Wang, S. Zhou, H. Zhu, J. Guo, Y. Chen, X. Li, Z. Dong, Q. Zhang and Y. Cong, *J. Colloid Interface Sci.*, 2025, **689**, 137263.
108 M. Xia, M. Yang, Y. Guo, X. Sun, S. Wang, Y. Feng and H. Ding, *ChemNanoMat*, 2022, **8**, e202200113.
109 W. Huang, J. Zhang, G. Deng, G. Zhu, Y. Chen, C. Xu and J. Cheng, *ACS Appl. Energy Mater.*, 2025, **8**, 2612–2619.
110 S. Cui, X. Zhong, Z. Li, P. Zhu, J. Hu, X. Zhou, P. Kidkhunthod, X. Wang, B. Mei and B. Xu, *Adv. Mater.*, 2025, **37**, 2504099.
111 C. Y. J. Lim, A. D. Handoko and Z. W. Seh, *Diamond Relat. Mater.*, 2022, **130**, 109461.
112 S. Y. Hsu, C. C. Chi, M. Y. Lu, S. Y. Chang, Y. T. Lai, S. Y. Tsai and J. G. Duh, *J. Alloys Compd.*, 2023, **947**, 169645.
113 S. A. Talas, P. D. Kolubah, R. Khairova, M. Alqahtani, S. I. El-Hout, F. M. Alissa, J. K. El-Demellawi, P. Castaño and H. O. Mohamed, *Mater. Horiz.*, 2025, **12**, 7648–7682.
114 T. Amrillah, A. R. Supandi, V. Puspasari, A. Hermawan and Z. W. Seh, *Trans. Tianjin Univ.*, 2022, **28**, 307–322.
115 M. Ozkan, K. A. M. Quiros, J. M. Watkins, T. M. Nelson, N. D. Singh, M. Chowdhury, T. Namboodiri, K. R. Talluri and E. Yuan, *Chem*, 2024, **10**, 443–483.
116 R. Morales-Salvador, J. D. Gouveia, Á. Morales-García, F. Viñes, J. R. B. Gomes and F. Illas, *ACS Catal.*, 2021, **11**, 11248–11255.
117 J. K. Pedersen, T. A. A. Batchelor, A. Bagger and J. Rossmeisl, *ACS Catal.*, 2020, **10**, 2169–2176.
118 Y. Sun, R. Yu, J. Sun, D. Legut, J. S. Francisco and R. Zhang, *J. Mater. Chem. A*, 2025, **13**, 11703–11716.
119 S. Cao, Y. Liu, Y. Hu, J. Li, C. Yang, Z. Chen, Z. Wang, S. Wei, S. Liu and X. Lu, *J. Colloid Interface Sci.*, 2023, **642**, 273–282.
120 X. Liu, L. Yao, S. Zhang, C. Huang and W. Yang, *Inorg. Chem.*, 2024, **63**, 6305–6314.
121 G. Sun, Y. Zhang, H. Xie, Y. He, C. Zhang, Y. Hu, E. Liu, C. He and A. B. Wong, *Nano Energy*, 2024, **132**, 110385.
122 A. Athawale, B. M. Abraham, M. V. Jyothirmai and J. K. Singh, *J. Phys. Chem. C*, 2023, **127**, 24542–24551.
123 Y. Luo, G. F. Chen, L. Ding, X. Chen, L. X. Ding and H. Wang, *Joule*, 2019, **3**, 279–289.
124 Y. Guo, T. Wang, Q. Yang, X. Li, H. Li, Y. Wang, T. Jiao, Z. Huang, B. Dong, W. Zhang, J. Fan and C. Zhi, *ACS Nano*, 2020, **14**, 9089–9097.
125 L. Zhou, D. Feng, Z. Li, Z. Lv, H. Li, C. Ge, X. Zhang and T. Ma, *ACS Appl. Mater. Interfaces*, 2025, **17**, 38050–38061.
126 Y. Lei, L. Zhang, X. Wang, D. Wang, Y. Zhao, B. Zhang, N. Zhang and H. Shang, *Chem. Sci.*, 2025, **16**, 18298–18308.
127 K. Chu, J. Qin, H. Zhu, M. De Ras, C. Wang, L. Xiong, L. Zhang, N. Zhang, J. A. Martens, J. Hofkens, F. Lai and T. Liu, *Sci. China Mater.*, 2022, **65**, 2711–2720.
128 Q. Zou, A. Qiu, Y. He, E. Y. Xue, L. Wang, G. Yang, Y. Shen, D. Luo, Q. Liu and D. K. P. Ng, *Adv. Sci.*, 2025, **12**, 2410537.
129 M. Naguib, R. R. Unocic, B. L. Armstrong and J. Nanda, *Dalton Trans.*, 2015, **44**, 9353–9358.
130 C. Xu, L. Wang, Z. Liu, L. Chen, J. Guo, N. Kang, X. L. Ma, H. M. Cheng and W. Ren, *Nat. Mater.*, 2015, **14**, 1135–1141.
131 M. Ghidiu, M. R. Lukatskaya, M. Q. Zhao, Y. Gogotsi and M. W. Barsoum, *Nature*, 2014, **516**, 78–81.
132 D. B. Velusamy, J. K. El-Demellawi, A. M. El-Zohry, A. Giugni, S. Lopatin, M. N. Hedhili, A. E. Mansour, E. Di Fabrizio, O. F. Mohammed and H. N. Alshareef, *Adv. Mater.*, 2019, **31**, 1807658.
133 M. R. Lukatskaya, S. Kota, Z. Lin, M. Q. Zhao, N. Shpigel, M. D. Levi, J. Halim, P. L. Taberna, M. W. Barsoum, P. Simon and Y. Gogotsi, *Nat. Energy*, 2017, **2**, 17105.
134 Y. Li, H. Shao, Z. Lin, J. Lu, L. Liu, B. Duployer, P. O. Å. Persson, P. Eklund, L. Hultman, M. Li, K. Chen, X. H. Zha, S. Du, P. Rozier, Z. Chai, E. Raymundo-Piñero, P. L. Taberna, P. Simon and Q. Huang, *Nat. Mater.*, 2020, **19**, 894–899.
135 C. Xu, L. Chen, Z. Liu, H. M. Cheng and W. Ren, in *2D Metal Carbides and Nitrides (MXenes)*, ed. B. Anasori and Y. Gogotsi, Springer, Cham, 2019, pp. 89–109.
136 Y. Yan, X. Huang, X. Yan, F. Zhang, J. Pan, J. Wu and J. M. Moradian, *Adv. Funct. Mater.*, 2025, **35**, 2420578.
137 F. Yang, K. L. Chan, Z. Wu, F. Zhao, M. C. Wong, S. Y. Pang and J. Hao, *Sci. China Mater.*, 2025, **68**, 2860–2867.
138 X. Gao, S. Zhang, J. Zhang, S. Wei, Y. Chen, Y. Zhang, W. Zheng, Z. Huang, B. Du, Z. Xie, B. Wang, J. Lin, J. Liu and Y. Ge, *Laser Photonics Rev.*, 2024, **18**, 2400082.
139 H. Zou, W. Zhang, F. Chen, C. Zhang, J. Zhang, L. Ren, W. Wang, F. Zhang and Z. Fu, *J. Adv. Ceram.*, 2026, **15**, 9221235.
140 Y. Wu, C. Chen, F. Pan, X. Li and W. Lu, *Chem. Eng. J.*, 2024, **499**, 156024.
141 W. Ma, M. Wang, Q. Yi, D. Huang, J. Dang, Z. Lv, X. Lv and S. Zhang, *Nano Energy*, 2022, **96**, 107129.
142 R. Iftikhar, Md. I. Kholil, S. Luo, M. A. Khan, M. Akter and A. Sinitskii, *Mater. Today Commun.*, 2026, **51**, 114598.
143 P. Urbankowski, B. Anasori, T. Makaryan, D. Er, S. Kota, P. L. Walsh, M. Zhao, V. B. Shenoy, M. W. Barsoum and Y. Gogotsi, *Nanoscale*, 2016, **8**, 11385–11391.
144 R. Meshkian, L.-Å. Näslund, J. Halim, J. Lu, M. W. Barsoum and J. Rosen, *Scr. Mater.*, 2015, **108**, 147–150.
145 B. Wei, Z. Fu, D. Legut, T. C. Germann, S. Du, H. Zhang, J. S. Francisco and R. Zhang, *Adv. Mater.*, 2021, **33**, 2102595.
146 P. Dadvari, W. H. Hung and K. W. Wang, *ACS Omega*, 2024, **9**, 27692–27698.